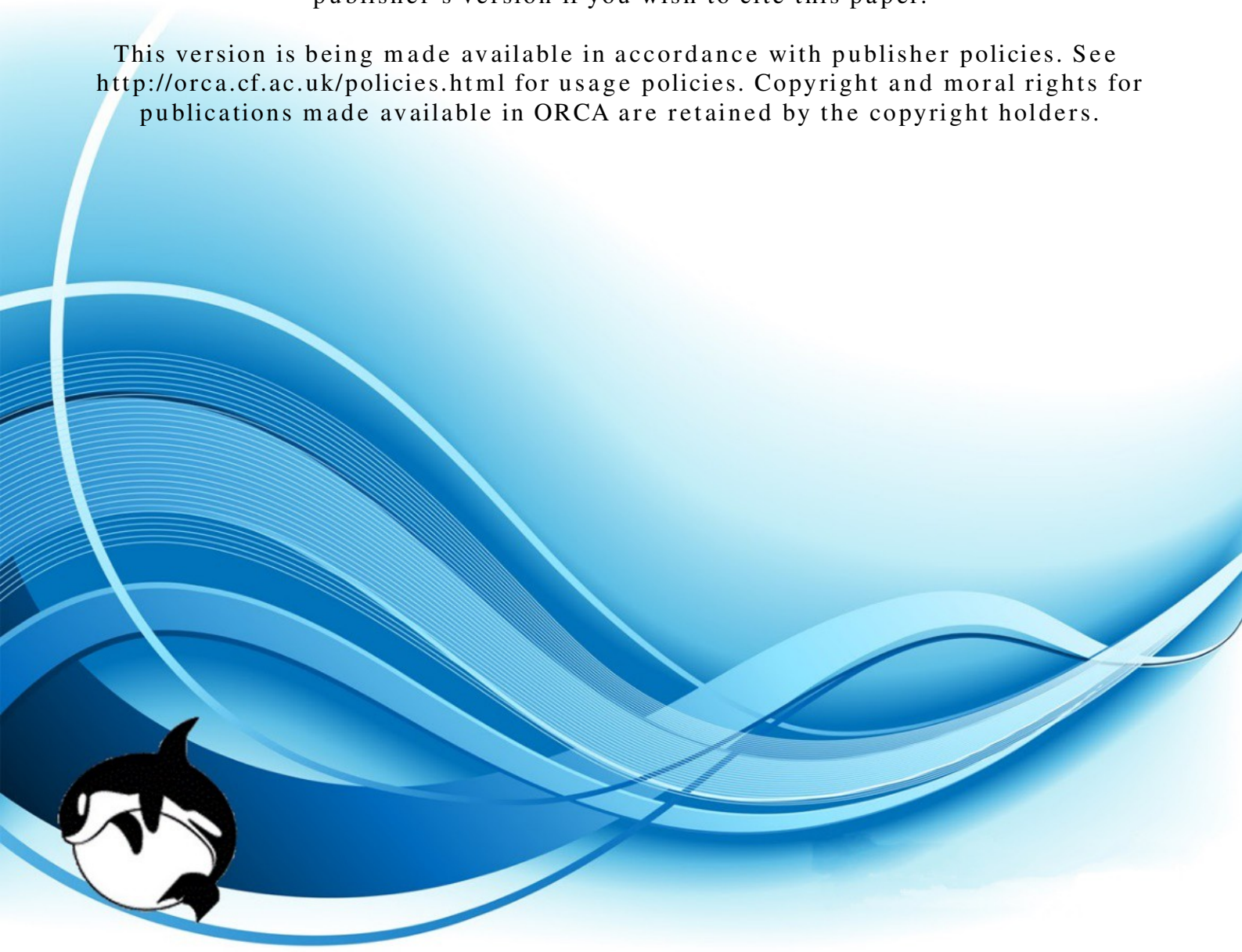

A one point integration rule over star convex polytopes

Amrita Francis, Sundararajan Natarajan
Department of Mechanical Engineering, Indian Institute of Technology Madras, India.

Elena Atroschchenko
Department of Mechanical Engineering, University of Chile, Santiago, Chile.

Bruno Lévy
Inria Nancy Grand-Est, Loria.

Stéphane PA Bordas
School of Engineering, Cardiff University, Wales, UK.
Institute of Computational Engineering, Faculty of Science Technology and Communication, University of Luxembourg, Luxembourg.

Abstract

The Linear Smoothing (LS) scheme [18] ameliorates linear and quadratic approximations over convex polytopes by employing a three-point integration scheme. In this work, we propose a linearly consistent one point integration scheme which possesses the properties of the LS scheme with three integration points but requires one third of the integration computational time. The essence of the proposed technique is to approximate the strain by the smoothed nodal derivatives that are determined by the discrete form of the divergence theorem. This is done by the Taylor's expansion of the weak form which facilitates the evaluation of the smoothed nodal derivatives acting as stabilization terms. The smoothed nodal derivatives are evaluated only at the centroid of each integration cell. These integration cells are the simplex subcells (triangle/tetrahedron in two and three dimensions) obtained by subdividing the polytope. The salient feature of the proposed technique is that it requires only n integrations for an $n-$sided polytope as opposed to $3n$ in [18] and $13n$ integration points in the conventional approach. The convergence properties, the accuracy, and the efficacy of the LS with one point integration scheme are discussed by solving few benchmark problems in elastostatics.

keywords: Polygonal finite element method, Wachspress shape functions, numerical integration, linear consistency, one point integration.

1 Introduction

Some of the constraints imposed by the conventional finite element method (FEM) is relaxed by the introduction of elements with arbitrary edges/faces. Approximations

on arbitrary polytopes have fueled the development of Polygonal/Polyhedral Finite Element Methods (PFEM) [39, 40, 45, 36]. POLY elements offer added flexibility in meshing complex geometries through various meshing algorithms using Voronoi tessellation [5, 46]. Such approaches were used to model complex geometries with inclusions [22], modeling of polycrystalline materials [43, 5, 23].

Adaptive mesh generation and regeneration such as local refinement and coarsening is also simplified with polytopes, since they naturally address the issues associated with hanging nodes [33, 34]. This has led researchers to develop methods with polygonal discretizations, for example, mimetic finite differences [26], virtual element method [11, 9, 10], finite volume method [13], discontinuous Galerkin method [7], virtual node method [21] and the scaled boundary finite element method [30, 35, 32]. Furthermore, polygonal/polyhedral elements have also been used to solve problems involving large deformations [2], incompressibility [46], contact problems [3] and fracture mechanics [24].

The flexibility provided by polytopes comes with challenges. First, the arbitrary polytopes usually rely on rational basis functions, i.e., the ratio of two polynomials. The construction of approximation functions over arbitrary polytopes is not unique. These approaches include: Mean value coordinates [17], Harmonic shape functions [4], Laplace basis functions [42] and maximum entropy basis functions [39]. Integrating such rational functions exactly is not possible in general. One approach to integrate over arbitrary polytopes is to sub-divide the region into triangles (in two dimensions) or tetrahedra (in three dimensions) and then employ conventional quadrature schemes. Although, the approach is simple, it requires *"many"* integration points to integrate even simple functions [42, 41, 44]. Moreover, the associated approximations do not pass the patch test [41, 44].

Inspired by the smoothing technique originally proposed for meshfree methods [8], a smoothing technique was proposed for polygonal elements in [12, 30]. However, it was shown that the direct application of the smoothing technique with average shape functions does not pass the patch test either and yields less accurate results [30].

Within the framework of the smoothed finite element method (SFEM), Francis *et al.,* [18] proposed a linear smoothing (LS) technique. The LS scheme employs $3n$ and $4n$ integration points for two and three dimensional elements, where n is the number of vertices of the polytope. It was shown with the help of numerical examples that the LS scheme leads to improved accuracy and recovers optimal convergence for the arbitrary convex polytopes. Moreover, it also passes the patch test to machine precision.

In this paper, we present a new one point quadrature rule over arbitrary star convex polytopes which can reproduce linear strain. In order to achieve this characteristic, the Taylor's expansion of the stiffness matrix and the strain-displacement matrix is employed around the center of the subcell. The modified derivatives are calculated at the centroid of each subcell and a conventional assembly procedure is adopted to calculate the stiffness matrix. The robustness, the accuracy and the convergence properties are studied with a few benchmark problems in elastostatics. The paper is organized as follows: Section 2 presents the governing equations for elasto-statics. The details of

the domain discretization with arbitrary polytopes is discussed in Section 3. Section 4 presents the new one point quadrature scheme for star convex arbitrary polytopes. Numerical results are presented in Section 5, followed by concluding remarks in the last section.

2 Governing equations for homogeneous linear elastic material

2.1 Strong form

Consider a homogeneous isotropic linear elastic body occupying $d = 2, 3$ dimensional space defined by an open domain $\Omega \subset \mathbb{R}^d$, bounded by the ($d$–1) dimensional surface Γ such that $\Gamma = \Gamma_u \cup \Gamma_t$ and $\emptyset = \Gamma_u \cap \Gamma_t$, where Γ_u and Γ_t are part of the boundary where Dirichlet and Neumann boundary conditions are specified, with $\mathbf{n}$ the unit outward normal. The boundary-value problem for linear elastostatics is defined by

$$\boldsymbol{\nabla} \cdot \boldsymbol{\sigma} + \mathbf{b} = \mathbf{0} \text{ in } \Omega, \tag{1}$$

with the following boundary conditions

$$\begin{aligned} \mathbf{u} &= \bar{\mathbf{u}} \text{ on } \Gamma_{\mathrm{u}}, \\ \boldsymbol{\sigma} \cdot \mathbf{n} &= \bar{\mathbf{t}} \text{ on } \Gamma_{\mathrm{t}}, \end{aligned} \tag{2}$$

where $\boldsymbol{\sigma}$ is the Cauchy stress tensor and $\mathbf{u} : \Omega \to \mathbb{R}^d$ is the nodal displacement field of the elastic body when it is subjected to external tractions $\bar{\mathbf{t}} : \Gamma_t \to \mathbb{R}^d$ and body forces $\mathbf{b} : \Omega \to \mathbb{R}^d$.

2.2 Weak form

We first define the infinite dimensional trial ($\mathscr{U}$) and test spaces ($\mathscr{V}^0$). Let $\mathcal{W}(\Omega)$ be the space including linear displacement fields.

$$\begin{aligned} \mathscr{U} &:= \left\{ \mathbf{u} \in [C^0(\Omega)]^d : \mathbf{u} \in [\mathcal{W}(\Omega)]^d \subseteq [H^1(\Omega)]^d,\ \mathbf{u} = \bar{\mathbf{u}} \text{ on } \Gamma_u \right\}, \\ \mathscr{V}^0 &:= \left\{ \mathbf{v} \in [C^0(\Omega)]^d : \mathbf{v} \in [\mathcal{W}(\Omega)]^d \subseteq [H^1(\Omega)]^d,\ \mathbf{v} = \mathbf{0} \text{ on } \Gamma_u \right\}. \end{aligned}$$

The Bubnov-Galerkin weak form is obtained by testing the strong form Equation (1) with the test functions in $\mathscr{V}^0$ and integrating over Ω. Using the divergence theorem and the fact that the test functions vanish on the Dirichlet boundary Γ_u, we obtain the weak form:

$$\text{Find} \quad \mathbf{u} \in \mathscr{U} \quad \text{such that, for all} \quad \mathbf{v} \in \mathscr{V}, \quad a(\mathbf{u}, \mathbf{v}) = \ell(\mathbf{v}), \tag{4a}$$

$$a(\mathbf{u}, \mathbf{v}) = \int_\Omega \boldsymbol{\sigma}(\mathbf{u}) : \boldsymbol{\varepsilon}(\mathbf{v}) \, \mathrm{d}V, \tag{4b}$$

$$\ell(\mathbf{v}) = \int_\Omega \mathbf{b} \cdot \mathbf{v} \, \mathrm{d}V + \int_{\Gamma_t} \hat{\mathbf{t}} \cdot \mathbf{v} \, \mathrm{d}S, \tag{4c}$$

where $\boldsymbol{\varepsilon} = \frac{1}{2}\left[\nabla\mathbf{u} + \nabla\mathbf{u}^{\mathrm{T}}\right]$ is the small strain tensor.

2.3 Discretisation

2.3.1 Discretised weak form

The domain Ω is partitioned into n_{el} non-overlapping polyhedral elements with planar faces. We define the discrete trial and test spaces by constructing shape functions over the union of all $n_{el} \in \Omega$. The shape functions ϕ_e are used to discretise the trial and test functions. These trial and test functions are written as a linear combination, over the union of all elements, of the shape functions ϕ_e with (vector) coefficients $\mathbf{u}_e$:

$$\begin{aligned} \mathbf{u}^h &= \sum_{e=1}^{n_{el}} \phi_e \mathbf{u}_e \\ \mathbf{v}^h &= \sum_{e=1}^{n_{el}} \phi_e \mathbf{v}_e \end{aligned} \tag{5}$$

The construction of these (Wachspress) shape functions is detailed in Section 2.3.2. With these notations, the following discrete weak form is obtained, which consists in finding $\mathbf{u}^h \in \mathscr{U}^h \subset \mathscr{U}$ such that for all discretised test functions $\mathbf{v}^h$ vanishing on the Dirichlet boundary (in set $\mathscr{V}^{0h} \subset \mathscr{V}^0$),

$$a(\mathbf{u}^h, \mathbf{v}^h) = \ell(\mathbf{v}^h) \tag{6}$$

which leads to the following system of linear equations:

$$\mathbf{K}\mathbf{u} = \mathbf{f} \tag{7}$$

$$\begin{aligned} \mathbf{K} &= \sum_h \mathbf{K}^h = \sum_h \int_{\Omega^h} \mathbf{B}^{\mathrm{T}}\mathbf{C}\mathbf{B}\,\mathrm{d}V, \\ \mathbf{f} &= \sum_h \mathbf{f}^h = \sum_h \left(\int_{\Omega^h} \boldsymbol{\phi}^{\mathrm{T}}\mathbf{b}\,\mathrm{d}V + \int_{\Gamma_t^h} \boldsymbol{\phi}^{\mathrm{T}}\hat{\mathbf{t}}\,\mathrm{d}S \right), \end{aligned}$$

where $\mathbf{K}$ is the global stiffness matrix, $\mathbf{f}$ is the global nodal force vector, $\mathbf{C}$ is the constitutive relation matrix for an isotropic linear elastic material and $\mathbf{B} = \boldsymbol{\nabla}\boldsymbol{\phi}$ is the strain-displacement matrix that is computed using the derivatives of the shape functions.

2.3.2 Construction of the shape functions

There are different ways to represent the shape functions over arbitrary polytopes [40]. In this paper, the Wachspress interpolants are used as the approximation functions to

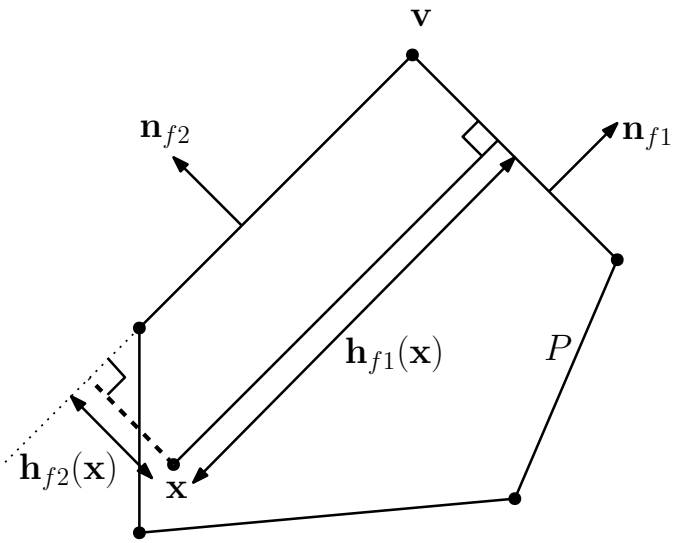

Figure 1: Barycentric coordinates: Wachspress basis function

describe the unknown fields. These functions are rational polynomials and the construction of the coordinates is as follows: Let $P \subset \mathbb{R}^3$ be a simple convex polyhedron with facets F and vertices V. For each facet $f \in F$, let $\mathbf{n}_f$ be the unit outward normal and for any $\mathbf{x} \in P$, let $h_f(\mathbf{x})$ denote the perpendicular distance of $\mathbf{x}$ to f, which is given by

$$h_f(\mathbf{x}) = (\mathbf{v} - \mathbf{x}) \cdot \mathbf{n}_f \tag{8}$$

for any vertex $\mathbf{v} \in V$ that belongs to f. For each vertex $\mathbf{v} \in V$, let f_1, f_2, f_3 be the three faces incident to $\mathbf{v}$ and for $\mathbf{x} \in P$, let

$$w_{\mathbf{v}}(\mathbf{x}) = \frac{\det(\mathbf{n}_{f_1}, \mathbf{n}_{f_2}, \mathbf{n}_{f_3})}{h_{f_1}(\mathbf{x}) h_{f_2}(\mathbf{x}) h_{f_3}(\mathbf{x})} \tag{9}$$

With a condition that the ordering of f_1, f_2, f_3 be anticlockwise around the vertex $\mathbf{v}$ when seen from outside P. Then the barycentric coordinates for $\mathbf{x} \in P$ is given by [48, 49]:

$$\phi_{\mathbf{v}}(\mathbf{x}) = \frac{w_{\mathbf{v}}(\mathbf{x})}{\sum\limits_{\mathbf{u} \in V} w_{\mathbf{u}}(\mathbf{x})}. \tag{10}$$

To deal with non-simple polyhedra, Warren *et al.,* [49] suggested that the non-simple vertex be decomposed into simple ones by perturbing its adjacent facets. This can also be accomplished by using *polar dual* with respect to each point $\mathbf{x}$ in $P \subset \mathbb{R}^3$, there exists a dual polyhedron,

$$\tilde{P}_x := \left\{ \mathbf{y} \in \mathbb{R}^3 : \mathbf{y}.(\mathbf{z} - \mathbf{x}) \leq 1, \mathbf{z} \in P \right\} \tag{11}$$

The dual polyhedron contains the origin and its vertices are the endpoints of the vectors $\mathbf{p}_f := \mathbf{n}_f / h_f(\mathbf{x})$. Let us suppose a vertex $\mathbf{v} \in V$ has k incident faces. The endpoints of

the k vectors form a k-sided polygon, which is the face of $\tilde{P}_x$. This face and the origin in $\mathbb{R}^3$ form a polygonal pyramid, $Q_{\mathbf{v}} \subset \tilde{P}_x$. Then, the functions, $\phi_{\mathbf{v}}$ in Equation (10) are barycentric coordinates, with $w_{\mathbf{v}}(\mathbf{x}) = \text{vol}(Q_{\mathbf{v}})$.

The Wachspress shape functions are the lowest order shape functions that satisfy boundedness, linearity and linear consistency on convex polytopes [48, 49]. On one front, the use of arbitrary shaped elements introduces flexibility and on another, it demands the construction of sufficiently accurate integration rules for computing the terms in the stiffness matrix. This is because the usual and standard integration rules cannot be employed directly. Some of the approaches to integrate over arbitrary polygons include: sub-triangulation [41], Green-Gauss quadrature [38], nodal quadrature [19], complex mapping [31], conforming interpolant quadrature and strain smoothing [8]. The aforementioned integration rules are restricted to two dimensions. In case of three dimensions, the polyhedron is sub-divided into tetrahedron and cubature rules over the tetrahedron are used for the purpose of numerical integration. Except for the strain smoothing technique, other approaches requires a lot of integration points for sufficient accuracy. In spite of this, it is inferred in [44] that the polygonal elements with existing integration technique do not satisfy patch test.

In author's earlier work [18], a linear smoothing technique was introduced that employed a linear smoothing function and required 3 integration points per subcell in two dimensions and four integration points per subcell in three dimensions. This is accompanied by a modified version of the strain-displacement matrix used to compute the stiffness matrix. The stiffness matrix, as computed within the framework of the SFEM is:

$$\tilde{\mathbf{K}} = \sum_h \tilde{\mathbf{K}}^h = \sum_h \int_{\Omega^h} \tilde{\mathbf{B}}^{\mathrm{T}} \mathbf{C} \tilde{\mathbf{B}} \, \mathrm{d}V, \tag{12}$$

The next section describes the method to generate arbitrary polyhedral meshes for complex geometries. Section 4 describes the new one point integration rule to integrate over the arbitrary polytopes.

3 Polyhedral meshing

3.1 Voronoi diagrams and Delaunay triangulations

In this section, we present the method that we use to generate the polyhedral meshes used in discretizing the domains used in the numerical examples (Section 5). To generate the polyhedral mesh, we follow a standard approach, that we detail below. To partition the domain $\Omega \subset \mathbb{R}^3$, we use a *Voronoi diagram*, defined as follows:

$$\begin{aligned} \text{Vor}(\mathbf{P}) &= \{\Omega_i\} \\ \Omega_i &= \{\mathbf{x} \in \Omega \mid \|\mathbf{x} - \mathbf{p}_i\|^2 \leq \|\mathbf{x} - \mathbf{p}_j\|^2 \quad \forall j \in (1 \dots n)\} \end{aligned} \tag{13}$$

where $\mathbf{P} = \{\mathbf{p}_i\}_{i=1}^n$ denotes a set of given points called the *generators* and where Ω is a 2D or 3D domain, defined by its polygonal or polyhedral boundary. Figure 2-left shows

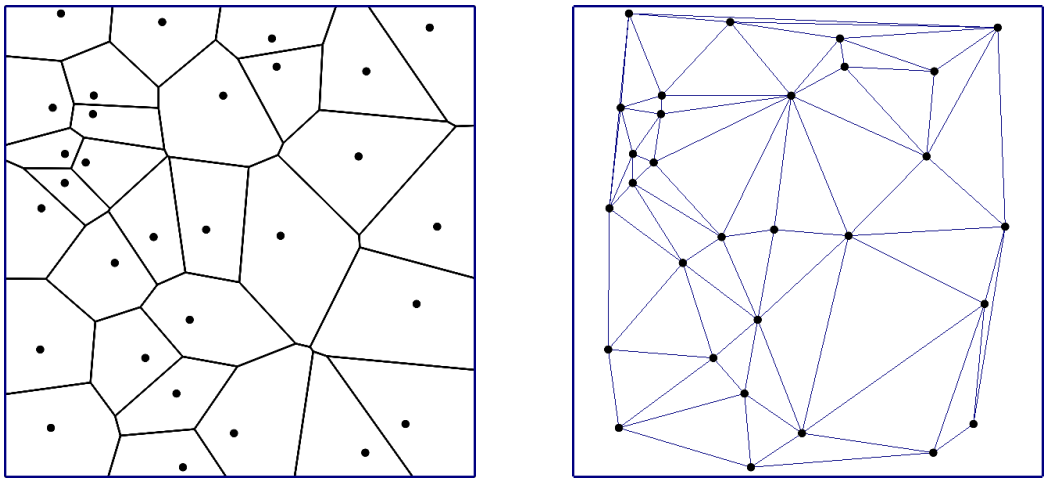

Figure 2: Left: an example of a Voronoi diagram; Right: the associated Delaunay triangulation. The domain Ω is a square.

an example of Voronoi diagram in 2D. Note that the Voronoi diagram is composed of cells with arbitrary number of edges, which requires complicated data structures. In 3D the situation is even worse: Voronoi cells are polyhedra with arbitrary number of faces and vertices. Therefore, from a practical point of view, it is easier to construct instead the dual structure, called the Delaunay triangulation, shown in Figure 2-right. The Delaunay triangulation, defined as the *combinatorial dual* of the Voronoi diagram. That is, the Delaunay triangulation is a simplicial set, that has an edge connecting two vertices $\mathbf{p}_i$ and $\mathbf{p}_j$ whenever the two Voronoi cells Ω_i and Ω_j have a common edge, and that has a triangle connecting three vertices $\mathbf{p}_i, \mathbf{p}_j, \mathbf{p}_k$ whenever the three Voronoi cells Ω_i,Ω_j and Ω_k have a common vertex. From the definition of the Voronoi cells, it is easy to see that the Delaunay triangles $\mathbf{p}_i, \mathbf{p}_j, \mathbf{p}_k$ are such that their circumscribed circle is empty of any other point $\mathbf{p}_l$. This property is exploited in the most popular algorithm, independently and simultaneously proposed by Bowyer [6] and Watson [50].

In our setting, now we need to answer the following questions, as will be done in the following two subsections:

1. Where should we place the generators $\mathbf{p}_i$ to obtain a *good* Voronoi diagram (and what is a good Voronoi diagram) ?

2. How to compute the Voronoi diagram for an arbitrarily domain Ω ?

3.2 Placing the generators $\mathbf{p}_i$

A regular Voronoi diagram can be obtained by placing the points $\mathbf{P}$ in such a way that the following objective function F is minimized:

$$F(\mathbf{P}) = \sum_{i=1}^{n} \int_{\Omega_i} \|\mathbf{x} - \mathbf{p}_i\|^2 d\mathbf{x}. \tag{14}$$

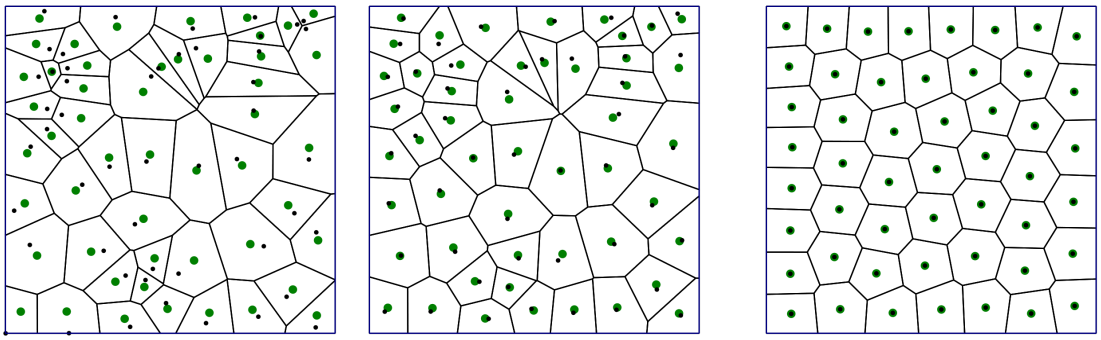

Figure 3: Two steps of Lloyd relaxation and the obtained centroidal Voronoi tessellation at convergence.

The objective function F, called the *quantization noise power*, corresponds to the inertia momenta of the Voronoi cells with respect to the points $\mathbf{p}_i$. From a signal point of view, it measures how well the point-set $\mathbf{P}$ samples the domain Ω [28].

To minimize the objective function F, it is interesting to derive its gradient with respect to one of the points $\mathbf{p}_i$. As one can see, it is non-trivial, because function F depends on integrals over the Ω_i regions, and the Ω_i regions depend in turn on the location of the points $\mathbf{p}_i$, therefore differentiating function F means differentiating integrals over moving domains, using for instance Reynolds's formula. A much shorter derivation path can be found: using the definition of the Voronoi cells (13), the objective function F is rewritten as follows:

$$F(\mathbf{P}) = \int_{\Omega} \min_i \|\mathbf{x} - \mathbf{p}_i\|^2 d\mathbf{x},$$

that is, the lower envelope of a family of functions. By the envelope theorem [29], its gradient at each point corresponds to the gradient of the function that realizes the min, and one directly obtains:

$$\frac{\partial F}{\partial \mathbf{p}_i} = 2m_i(\mathbf{p}_i - \mathbf{g}_i) \quad \text{where:} \quad \left\{ \begin{array}{rcl} m_i & = & \int_{\Omega_i} d\mathbf{x} \\ \mathbf{g}_i & = & (1/m_i) \int_{\Omega_i} \mathbf{x} d\mathbf{x} \end{array} \right. \tag{15}$$

Thus, the stationary points of F are such that each generator $\mathbf{p}_i$ coincides with the centroid $\mathbf{g}_i$ of its Voronoi cell, hence the name *centroidal Voronoi tessellation* (or CVT for short) that qualify such a configuration. To compute such a CVT, gradient descent is a natural idea that comes to mind. It was initially proposed to iteratively move the generators to the centroids [28]. This idea, known as *Lloyd relaxation* is demonstrated in Figure 3, where the generators are symbolized as small black dots and the centroids of the Voronoi cells as large green dots. As can be seen, moving the generators to the centroids iteratively improves the regularity of the Voronoi diagram. This behavior was later studied [14], and it was proved that moving the generators to the centroids always decreases the value of F. Thus, Lloyd relaxation can be understood as a gradient

descent method that does not require step-length control. Finally, the regularity of F was analyzed [27] and its C^2 smoothness allowed to design a quasi-Newton algorithm with faster speed of convergence.

To summarize the answer to the initial question, we place the generators as follows: first starting from a uniform random distribution, we then optimize the generators by minimizing F. We use the efficient quasi-Newton algorithm. One can also use Lloyd relaxation, that simply means iteratively relocating the generators to the centroids of the Voronoi cells.

3.3 Voronoi diagram in an arbitrary domain

Computing a Centroidal Voronoi Tessellation, as explained in the previous subsection, requires to compute a series of Voronoi diagram, as well as the masses and centroids of the Voronoi cells. It is easy to see that the Voronoi cells are defined as the intersection between half-spaces and the domain Ω:

$$\begin{aligned}
\Omega_i &= \{\mathbf{x} \in \Omega \mid \|\mathbf{x}-\mathbf{p}_i\|^2 \leq \|\mathbf{x}-\mathbf{p}_j\|^2 \quad \forall j \in (1 \dots n)\} \\
&= \Omega \cap \left(\bigcap_{i=1}^{n} \Pi^+(\mathbf{p}_i, \mathbf{p}_j) \right) \\
\text{where} \quad \Pi^+(\mathbf{p}_i, \mathbf{p}_j) &= \{\mathbf{x} \in \mathbb{R}^3 \quad | \quad \|\mathbf{x}-\mathbf{p}_i\|^2 \leq \|\mathbf{x}-\mathbf{p}_j\|^2\}
\end{aligned}$$

Computing the intersection between the half-spaces Π^+ is easy, however, the main difficulty is that the domain Ω that we use is in general non-convex, which can lead to both very complicated combinatorial configurations and problems with numerical precision. Therefore, we decompose the domain Ω into tetrahedra. We used Tetgen [37] in the examples shown here. Then, to compute the Voronoi cells, the only operation that we need is the intersection between a tetrahedron and a half-space. An example is shown in Figure 4, with both the initial tetrahedral mesh and its intersection with the Voronoi diagram. The intersection mesh is computed using a specialized algorithm [51], based on geometric predicates in arbitrary precision [25] that overcome numerical precision problems and degeneracies.

To obtain the final mesh, the Voronoi cells are assembled from all the volumetric parts corresponding to intersections with the initial tetrahedral mesh, that is, the edges displayed in the closeup in Figure 4 are discarded.

Our method may seem at first sight more complicated than directly computing the intersection between the Voronoi diagram and the interior of Ω, but to our knowledge, there is no existing algorithm to do so *reliably*. Our algorithm decomposes the problem into simpler convex $\cap$ convex intersections, that can be exactly computing, freely of numerical precision problems.

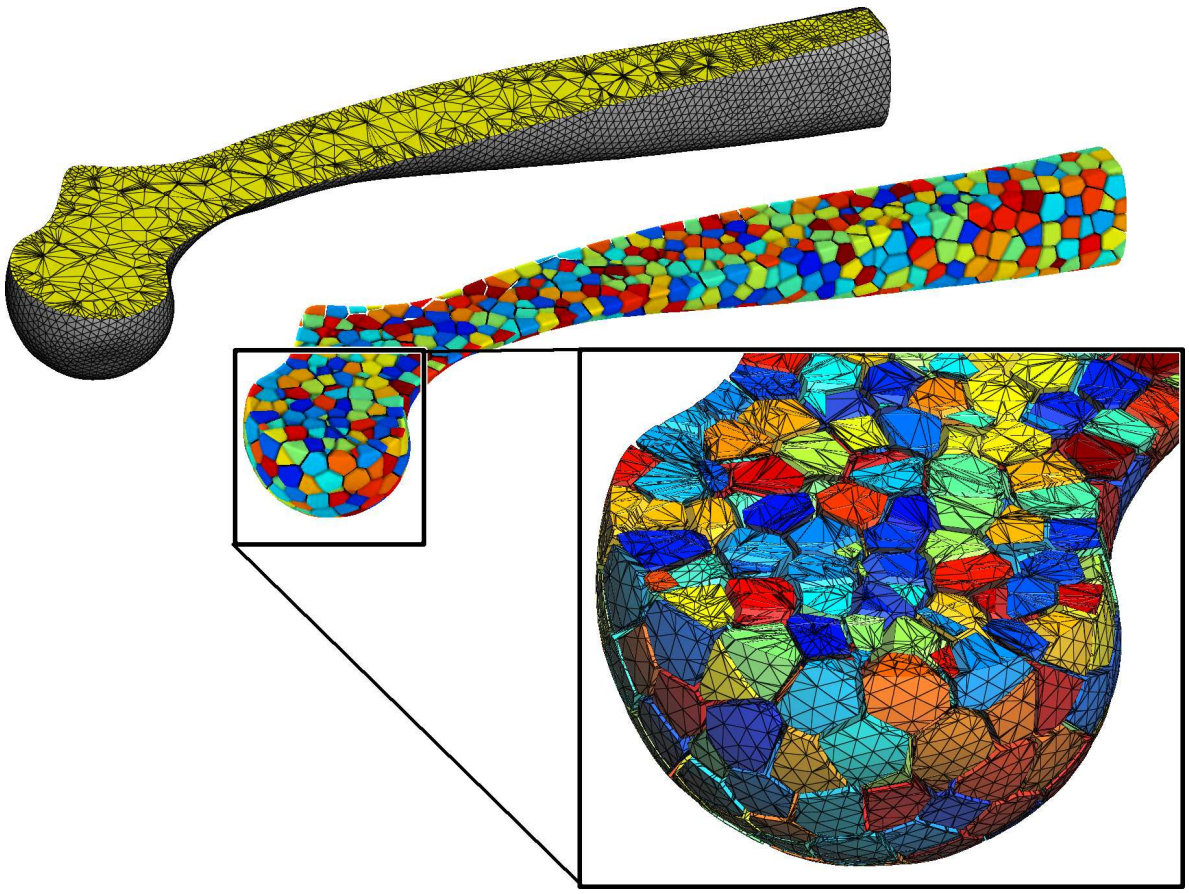

Figure 4: Voronoi meshing of a femur. Top: initial tetrahedral mesh; Bottom: generated Voronoi diagram and its intersection with the tetrahedral mesh.

4 One point quadrature scheme

In this section, a new numerical integration scheme is proposed to numerically integrate over the star convex arbitrary polygon and polyhedron inspired from the work of Duan *et al.,* [20]. We restrict ourselves to cell-based smoothing technique, wherein the physical element is sub-divided into simplex elements. This sub-division is solely for the purpose of numerical integration and does not introduce additional degrees of freedom. In this paper, triangles and tetrahedra in two and three dimensions are used as simplex elements. Similar to our earlier work, a linear smoothing function is employed, however, only one integration point is used to compute the modified derivative. This is depicted in Figure 5. For sake of brevity and simplicity of the notation, the derivation of the proposed smoothing scheme is given in detail only for two-dimensions using the Cartesian coordinate system. The extension to three dimensions is straight forward and interested readers are referred to the corresponding author to obtain the MATLAB code.

Within the SFEM framework, the discrete modified strain field $\tilde{\varepsilon}_{ij}^{h}$ that yields the

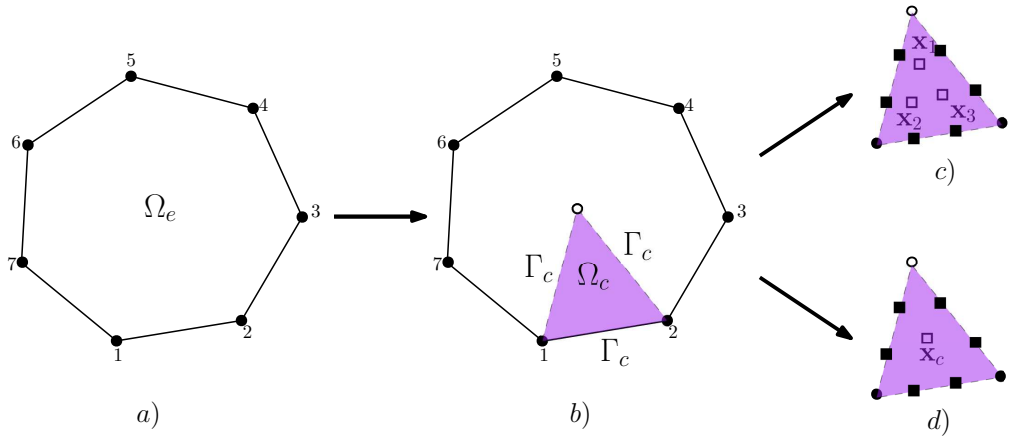

(a) Discertization of arbitrary polygon into triangular subcell using virtual point shown by 'open' circle.

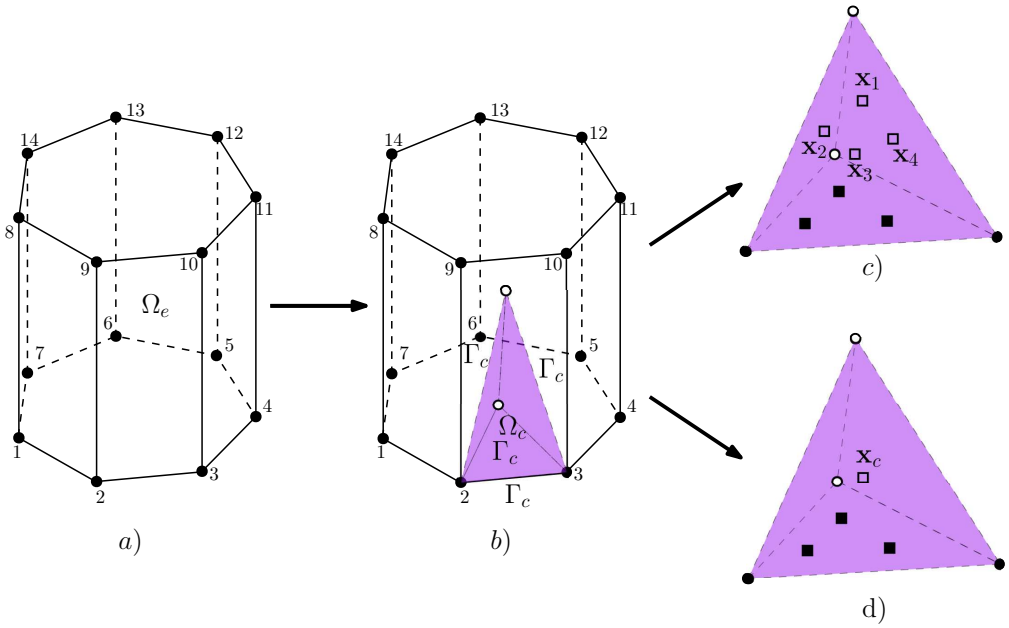

(b) Discertization of arbitrary polyhedron into tetrahedral subcell using virtual point shown by 'open' circle.

Figure 5: Schematic representation of the three point and one point integration techniques. The nodes are depicted by the filled circles, while the Gauss point per edge/face is shown by filled squares. The smoothed derivatives are computed at the 'open' squares over each smoothing cell denoted by Ω_c.

modified strain-displacement matrix ($\tilde{\mathbf{B}}$) which is then used to build the stiffness matrix is related to the compatible strain field ε_{ij}^h by:

$$\tilde{\varepsilon}_{ij}^h(\mathbf{x}) = \int_{\Omega_C^h} \varepsilon_{ij}^h(\mathbf{x})\ \mathbf{q}(\mathbf{x}) \mathrm{d}V \tag{16}$$

where $q(\mathbf{x})$ is the smoothing function. On writing Equation (16) at the basis functions derivative level and invoking Gauss-Ostrogradsky theorem, we get:

$$\int_{\Omega_C^h} \phi_{I,x}\ \mathbf{q}(\mathbf{x})\, \mathrm{d}V = \int_{\Gamma_C^h} \phi_I\ \mathbf{q}(\mathbf{x}) n_j\, \mathrm{d}S - \int_{\Omega_C^h} \phi_I\ \mathbf{q}_{,x}(\mathbf{x})\, \mathrm{d}V \tag{17}$$

In this work, a linear smoothing function $\mathbf{q}(\mathbf{x}) = \{1,\ x,\ y\}$ in two dimensions and $\mathbf{q}(\mathbf{x}) = \{1,\ x,\ y,\ z\}$ in three dimensions is employed and numerical integration is employed to evaluate the terms in Equation (17). Note that the domain integral in Equation (17) is evaluated at the center of the subcell, $\mathbf{x}_c = (x_c, y_c)$ (see Figure 5. The center of the subcell is denoted by 'open' circle), whilst, the boundary integral is evaluated along the boundary of the subcell (the location of integration point on the boundary is represented by 'filled' square in Figure 5). However, this will lead to a singular system [16, 15]. This is circumvented by introducing higher order derivatives, viz., $\tilde{\phi}_{I,x}(x_c), \tilde{\phi}_{I,xx}(x_c), \tilde{\phi}_{I,xy}(x_c)$ by using Taylor's expansion of the modified derivatives around the center of the subcell, $\mathbf{x}_c$. The Taylor's expansion (around the center of the subcell $\mathbf{x}_c$) of $\tilde{\phi}_{I,x}(\mathbf{x})$, $\mathbf{q}(\mathbf{x})$ and $\phi_I(\mathbf{x})$, used is defined as:

$$\tilde{\phi}_{I,x}(\mathbf{x}) = \tilde{\phi}_{I,x}(\mathbf{x}_c) + (x - x_c)\tilde{\phi}_{I,xx}(\mathbf{x}_c) + (y - y_c)\tilde{\phi}_{I,xy}(\mathbf{x}_c) + \mathcal{O}((\mathbf{x} - \mathbf{x}_c)^2) \tag{18a}$$

$$\mathbf{q}(\mathbf{x}) = \mathbf{q}(\mathbf{x}_c) + (x - x_c)\mathbf{q}_{,x}(\mathbf{x}_c) + (y - y_c)\mathbf{q}_{,y}(\mathbf{x}_c) \tag{18b}$$

$$\begin{aligned}\phi_I(\mathbf{x}) = \phi_I(\mathbf{x}_c) + (x - x_c)\phi_{I,x}(\mathbf{x}_c) + (y - y_c)\phi_{I,y}(\mathbf{x}_c) + \frac{1}{2}(x - x_c)^2\phi_{I,xx}(\mathbf{x}_c) \\ + (x - x_c)(y - y_c)\phi_{I,xy}(\mathbf{x}_c) + \frac{1}{2}(y - y_c)^2\phi_{I,yy}(\mathbf{x}_c) + \mathcal{O}((\mathbf{x} - \mathbf{x}_c)^3)\end{aligned} \tag{18c}$$

Upon substituting Equation (18) into Equation (17), we obtain:

$$\begin{aligned}&\mathbf{q}(\mathbf{x}_c)A\tilde{\phi}_{I,x}(\mathbf{x}_c) + \left[\mathbf{q}_{,x}(\mathbf{x}_c)I_c^{xx} + \mathbf{q}_{,y}(\mathbf{x}_c)I_c^{xy}\right]\tilde{\phi}_{I,xx}(\mathbf{x}_c) + \left[\mathbf{q}_{,x}(\mathbf{x}_c)I_c^{xy} + \mathbf{q}_{,y}(\mathbf{x}_c)I_c^{yy}\right]\tilde{\phi}_{I,xy}(\mathbf{x}_c) \\ &\quad = \int_{\Gamma_c^h} \phi_I(\mathbf{x})\mathbf{q}(\mathbf{x})\mathbf{n}\ \mathrm{d}\Gamma - \left[A\phi_I(\mathbf{x}_c) + \frac{1}{2}I_c^{xx}\phi_{I,xx}(\mathbf{x}_c) + I_c^{xy}\phi_{I,xy}(\mathbf{x}_c) + \frac{1}{2}I_c^{yy}\phi_{I,yy}(\mathbf{x}_c)\right]\end{aligned} \tag{19}$$

where $A = \int_{\Omega_c^h} \mathrm{d}\Omega$ is the area of the integration domain Ω. The first order area moments with respect to cell center $\mathbf{x}_c$ vanish and the second order area moments are given by:

$$\left\{\begin{array}{c} I_c^{xx} \\ I_c^{xy} \\ I_c^{yy} \end{array}\right\} = \int_{\Omega_c} \left\{\begin{array}{c} (x - x_c)^2 \\ (x - x_c)(y - y_c) \\ (y - y_c)^2 \end{array}\right\} \mathrm{d}\Omega \tag{20}$$

Remark 1 *For a regular polygon, the second order area moment I_c^{xy} also vanish apart from the first order area moments.*

Remark 2 *Equation (21) always have an unique solution provided the triangles do not degenerate to a line.*

This now leads to the following system of linear equations:

$$\mathbf{W}\mathbf{d}_j = \mathbf{g}_j, \quad j = 1, 2 \tag{21}$$

where,

$$\mathbf{W} = \begin{bmatrix} A & 0 & 0 \\ Ax_c & I_c^{xx} & I_c^{xy} \\ Ay_c & I_c^{xy} & I_c^{yy} \end{bmatrix}$$

$$\mathbf{g}_1 = \left\{ \begin{array}{c} \sum_{L=1}^{3} \sum_{G=1}^{2} \phi_I(\mathbf{x}_G) n_x^L w_G \\ \sum_{G=1}^{2} \phi_I(\mathbf{x}_G) x_G n_x^L w_G - F_g \\ \sum_{G=1}^{2} \phi_I(\mathbf{x}_G) y_G n_y^L w_G \end{array} \right\}$$

$$\mathbf{g}_2 = \left\{ \begin{array}{c} \sum_{L=1}^{3} \sum_{G=1}^{2} \phi_I(\mathbf{x}_G) n_x^L w_G \\ \sum_{G=1}^{2} \phi_I(\mathbf{x}_G) x_G n_x^L w_G \\ \sum_{G=1}^{2} \phi_I(\mathbf{x}_G) y_G n_y^L w_G - F_g \end{array} \right\} \tag{22}$$

where

$$F_g = A\phi_I(\mathbf{x}_c) + \frac{1}{2} I_c^{xx} \phi_{I,xx}(\mathbf{x}_c) + I_c^{xy} \phi_{I,xy}(\mathbf{x}_c) + \frac{1}{2} I_c^{yy} \phi_{I,yy}(\mathbf{x}_c)$$

where $\phi_I(\mathbf{x}_c)$, $\phi_{I,xx}(\mathbf{x}_c)\, \phi_{I,yy}(\mathbf{x}_c)$ and $\phi_{I,xy}(\mathbf{x}_c)$ are the barycentric coordinates and its derivatives are evaluated at the center of the cell, $(x_G,\ y_G)$ and w_G are the integration points and the weights respectively, along the boundary of the smoothing cells (see Figure 5. The integration points are shown as filled square) and n_x^L and n_y^L are the outward normals along the boundary of the smoothing cell. The solution vector is given by:

$$\mathbf{d}_1 = \left\{ \begin{array}{c} \tilde{\phi}_{I,x}(\mathbf{x}_c) \\ \tilde{\phi}_{I,xx}(\mathbf{x}_c) \\ \tilde{\phi}_{I,xy}(\mathbf{x}_c) \end{array} \right\} \tag{23a}$$

$$\mathbf{d}_2 = \left\{ \begin{array}{c} \tilde{\phi}_{I,y}(\mathbf{x}_c) \\ \tilde{\phi}_{I,yx}(\mathbf{x}_c) \\ \tilde{\phi}_{I,yy}(\mathbf{x}_c) \end{array} \right\} \tag{23b}$$

This is further used to construct the modified strain displacement matrix and its derivatives used to evaluate the stiffness matrix as:

$$\tilde{\mathbf{B}} = \begin{bmatrix} \tilde{\mathbf{B}}_1 & \tilde{\mathbf{B}}_2 & .... & \tilde{\mathbf{B}}_n \end{bmatrix} \tag{24}$$

$$\tilde{\mathbf{B}}_I(\mathbf{x}_c) = \begin{bmatrix} \tilde{\phi}_{I,x}(\mathbf{x}_c) & 0 \\ 0 & \tilde{\phi}_{I,y}(\mathbf{x}_c) \\ \tilde{\phi}_{I,y}(\mathbf{x}_c) & \tilde{\phi}_{I,x}(\mathbf{x}_c) \end{bmatrix} \tag{25}$$

$$\frac{\partial \tilde{\mathbf{B}}_I(\mathbf{x}_c)}{\partial x} = \begin{bmatrix} \tilde{\phi}_{I,xx}(\mathbf{x}_c) & 0 \\ 0 & \tilde{\phi}_{I,yx}(\mathbf{x}_c) \\ \tilde{\phi}_{I,yx}(\mathbf{x}_c) & \tilde{\phi}_{I,xx}(\mathbf{x}_c) \end{bmatrix} \tag{26}$$

$$\frac{\partial \tilde{\mathbf{B}}_I(\mathbf{x}_c)}{\partial y} = \begin{bmatrix} \tilde{\phi}_{I,xy}(\mathbf{x}_c) & 0 \\ 0 & \tilde{\phi}_{I,yy}(\mathbf{x}_c) \\ \tilde{\phi}_{I,yy}(\mathbf{x}_c) & \tilde{\phi}_{I,xy}(\mathbf{x}_c) \end{bmatrix} \tag{27}$$

It should be noted that in the proposed technique the smoothed nodal derivatives are used to compute the terms in the modified stiffness matrix. To introduce the higher order modified derivatives into the final discretized form (see Equation (12)), the stiffness matrix is expanded in Taylor's series (around the center of the subcell, $\mathbf{x}_c$) as:

$$\tilde{\mathbf{K}}^{\mathbf{\Omega_c}} = \int_{\Omega_c} \tilde{\mathbf{B}}^{\mathrm{T}} \mathbf{C} \tilde{\mathbf{B}} \, \mathrm{d}V, \tag{28a}$$

$$= \int_{\Omega_c} \left[\tilde{\mathbf{B}}^{\mathrm{T}} + \frac{\partial \tilde{\mathbf{B}}^{\mathrm{T}}}{\partial x}(x - x_c) + \frac{\partial \tilde{\mathbf{B}}^{\mathrm{T}}}{\partial y}(y - y_c) \right] \mathbf{C} \left[\tilde{\mathbf{B}}^{\mathrm{T}} + \frac{\partial \tilde{\mathbf{B}}^{\mathrm{T}}}{\partial x}(x - x_c) + \frac{\partial \tilde{\mathbf{B}}^{\mathrm{T}}}{\partial y}(y - y_c) \right] \mathrm{d}V, \tag{28b}$$

However, to compute the body forces, standard Wachspress interpolants and its higher order derivatives are employed. The body force is computed as follows:

$$\tilde{\mathbf{f}}^{\mathbf{b}} = \int_{\Omega_c} \left(\boldsymbol{\phi}^{\mathrm{T}} \mathbf{b} \right) \mathrm{d}V, \tag{29a}$$

$$= \int_{\Omega_c} \Big\{ \boldsymbol{\phi}^{\mathrm{T}} \mathbf{b}|_{(\mathbf{x}_c)} + \frac{\partial \boldsymbol{\phi}^{\mathrm{T}}}{\partial x} \mathbf{b}|_{(\mathbf{x}_c)}(x - x_c) + \frac{\partial \boldsymbol{\phi}^{\mathrm{T}}}{\partial y} \mathbf{b}|_{(\mathbf{x}_c)}(y - y_c)$$

$$+ \frac{1}{2} \frac{\partial^2 \boldsymbol{\phi}^{\mathrm{T}}}{\partial x^2} \mathbf{b}|_{(\mathbf{x}_c)}(x - x_c)^2 + \frac{1}{2} \frac{\partial^2 \boldsymbol{\phi}^{\mathrm{T}}}{\partial y^2} \mathbf{b}|_{(\mathbf{x}_c)}(y - y_c)^2 \tag{29b}$$

$$+ \frac{\partial^2 \boldsymbol{\phi}^{\mathrm{T}}}{\partial x \partial y} \mathbf{b}|_{(\mathbf{x}_c)}(x - x_c)(y - y_c) \Big\} \, \mathrm{d}V,$$

$$= \mathbf{A} \boldsymbol{\phi}^{\mathrm{T}} \mathbf{b}|_{(\mathbf{x}_c)} + \frac{1}{2} I_c^{xx} \frac{\partial^2 \boldsymbol{\phi}^{\mathrm{T}}}{\partial x^2} \mathbf{b}|_{(\mathbf{x}_c)} + \frac{1}{2} I_c^{yy} \frac{\partial^2 \boldsymbol{\phi}^{\mathrm{T}}}{\partial y^2} \mathbf{b}|_{(\mathbf{x}_c)} + I_c^{xy} \frac{\partial^2 \boldsymbol{\phi}^{\mathrm{T}}}{\partial x \partial y} \mathbf{b}|_{(\mathbf{x}_c)} \tag{29c}$$

The stiffness matrix with the modified derivatives and the body force vector with the higher order derivatives are substitute in Equation (7) to compute the unknown displacement field.

5 Numerical examples

In this section, we demonstrate the accuracy and the convergence properties of the proposed linear smoothing scheme (LS) over arbitrary polytopes using $1n$ integration point. The LS1 scheme is compared to the The LS3n scheme by solving few benchmark problems. We also demonstrate the performance of the proposed scheme in three-dimensional elasticity problems. In all the numerical examples, we discretize the domain with arbitrary polytopes based on centroid Voronoi tessellation. The two dimensional polygonal meshes are generated by using the built-in Matlab function voronoin and the Matlab functions in Polytop [45]. For three dimensional problems, the polyhedral meshes are generated based on the approach discussed in 3. For the purpose of error estimation and convergence studies, the L^2 norm and H^1 seminorm of the error are used. The following convention is used while discussing the results:

- LS3n-2D, LS3n-3D: linear smoothing scheme with three point integration rule over arbitrary polytopes, in two and in three dimensions, respectively.
- LS1-2D, LS1-3D: linear smoothing scheme with one point integration rule over arbitrary polytopes, in two and three dimensions, respectively.

In the first example, the accuracy and the convergence properties of the proposed one point quadrature (LS1-2D, LS1-3D) is demonstrated with a linear patch test. The following displacements are prescribed on the boundary in the two-dimensional case:

$$\begin{pmatrix} \hat{u} \\ \hat{v} \end{pmatrix} = \begin{pmatrix} 0.1 + 0.1x + 0.2y \\ 0.05 + 0.15x + 0.1y \end{pmatrix} \tag{30}$$

and in the three-dimensional case the following displacements are prescribed on the boundary:

$$\begin{pmatrix} \hat{u} \\ \hat{v} \\ \hat{w} \end{pmatrix} = \begin{pmatrix} 0.1 + 0.1x + 0.2y + 0.2z \\ 0.05 + 0.15x + 0.1y + 0.2z \\ 0.05 + 0.1x + 0.2y + 0.2z \end{pmatrix}. \tag{31}$$

The exact solution to Equation (1) is $\mathbf{u} = \hat{\mathbf{u}}$ in the absence of body forces. The domain is discretized with arbitrary polygonal and polyhedral finite elements. Figure 6 and Figure 7 shows a few representative meshes used for the two and three dimensional studies, respectively. The errors in the L^2 norm and the H^1 seminorm for the LS3n schemes and the proposed LS1 one point quadrature are shown in Table 1 for two-dimensions and in Table 2 for three dimensions. It can be seen that the proposed one point quadrature scheme passes the linear patch test to machine precision for both polygonal and polyhedral discretizations.

Next, the convergence properties and the accuracy of the proposed technique is studied when the following higher order displacements are prescribed on the boundaries:

$$\begin{pmatrix} \hat{u} \\ \hat{v} \end{pmatrix} = \begin{pmatrix} 0.1x^2 + 0.1xy + 0.2y^2 \\ 0.05x^2 + 0.15xy + 0.1y^2 \end{pmatrix}, \tag{32}$$

Table 1: Relative error in the L^2 norm and H^1 seminorm for the two-dimensional linear patch test.

Mesh	LS3n-2D		LS1-2D	
(c.f. Figure 6)	L^2	H^1	L^2	H^1
a	5.38×10^{-14}	2.84×10^{-11}	8.38×10^{-15}	2.96×10^{-13}
b	1.93×10^{-13}	4.43×10^{-11}	7.62×10^{-14}	4.79×10^{-12}
c	2.01×10^{-13}	7.01×10^{-11}	1.43×10^{-13}	1.28×10^{-11}
d	2.96×10^{-13}	1.02×10^{-10}	2.71×10^{-13}	2.76×10^{-11}

Table 2: Error in the L^2 norm and H^1 seminorm for the three-dimensional linear patch test.

Number of	LS3n-3D		LS1-3D	
elements	L^2	H^1	L^2	H^1
9	2.03×10^{-12}	3.34×10^{-10}	2.98×10^{-11}	2.23×10^{-10}
25	1.92×10^{-12}	1.75×10^{-10}	7.38×10^{-10}	5.56×10^{-09}
100	2.66×10^{-12}	4.93×10^{-10}	2.08×10^{-10}	2.13×10^{-09}
300	3.21×10^{-12}	3.11×10^{-10}	7.73×10^{-10}	1.28×10^{-09}

in the two-dimensional case and the following in the three-dimensional case:

$$\begin{pmatrix}\hat{u}\\ \hat{v}\\ \hat{w}\end{pmatrix} = \begin{pmatrix} 0.1+0.2x+0.2x+0.1z+0.15x^2+0.2y^2+0.1z^2+0.15xy+0.1yz+0.1zx \\ 0.15+0.1x+0.1y+0.2z+0.2x^2+0.15y^2+0.1z^2+0.2xy+0.1yz+0.2zx \\ 0.15+0.15x+0.2y+0.1z+0.15x^2+0.1y^2+0.2z^2+0.1xy+0.2yz+0.15zx \end{pmatrix} \tag{33}$$

The exact solution to Equation (1) is $\mathbf{u} = \hat{\mathbf{u}}$ when the body is subjected to the body forces:

$$\mathbf{b} = \begin{pmatrix} -0.2\mathbf{C}(1,1) - 0.15\mathbf{C}(1,2) - 0.55\mathbf{C}(3,3) \\ -0.1\mathbf{C}(1,2) - 0.2\mathbf{C}(2,2) - 0.2\mathbf{C}(3,3) \end{pmatrix}, \tag{34}$$

in two-dimensions and

$$\mathbf{b} = \begin{pmatrix} -0.3\mathbf{C}(1,1) - 0.2\mathbf{C}(1,2) - 0.15\mathbf{C}(1,3) - 0.6\mathbf{C}(4,4) - 0.35\mathbf{C}(6,6) \\ -0.15\mathbf{C}(1,2) - 0.3\mathbf{C}(2,2) - 0.2\mathbf{C}(2,3) - 0.55\mathbf{C}(4,4) - 0.4\mathbf{C}(5,5) \\ 0.1\mathbf{C}(1,3) - 0.1\mathbf{C}(2,3) - 0.4\mathbf{C}(3,3) - 0.3\mathbf{C}(5,5) - 0.4\mathbf{C}(6,6) \end{pmatrix} \tag{35}$$

in three dimensions, where $\mathbf{C}$ is the constitutive matrix. The domain is discretized with arbitrary polygonal and polyhedral finite elements. Figure 6 and Figure 7 shows a few representative meshes used for the two and three dimensional studies, respectively. Figure 8 shows the convergence rates when the domain is discretized with polytope linear elements. It can be inferred that the proposed one point quadrature scheme yields optimal convergence rates in two and in three dimensions.

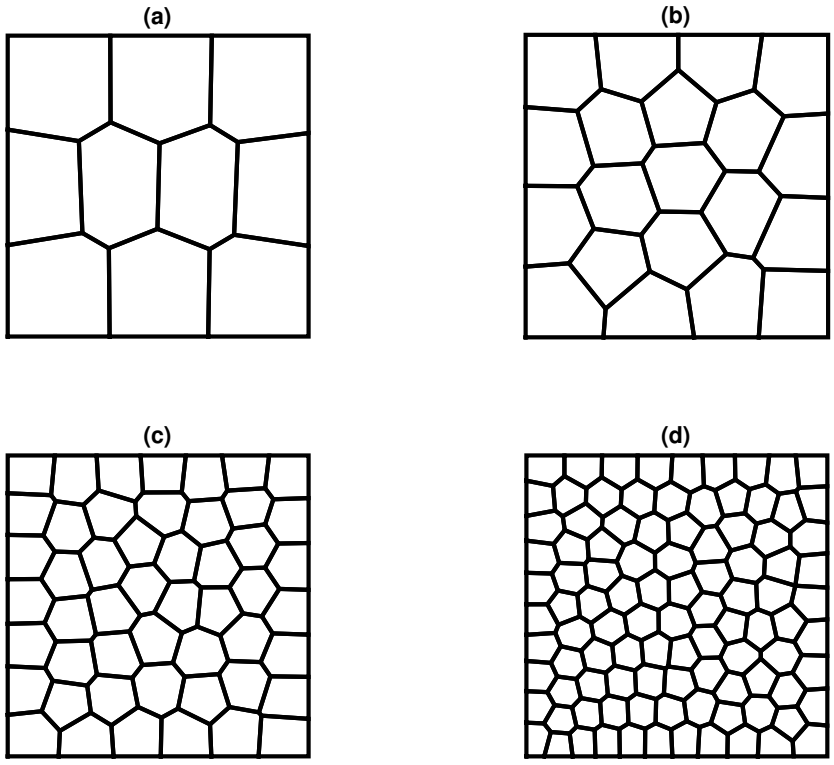

Figure 6: Square domain discretized with polygonal elements. Representative meshes containing (a) 10, (b) 20, (c) 50 and (d) 100 polygons.

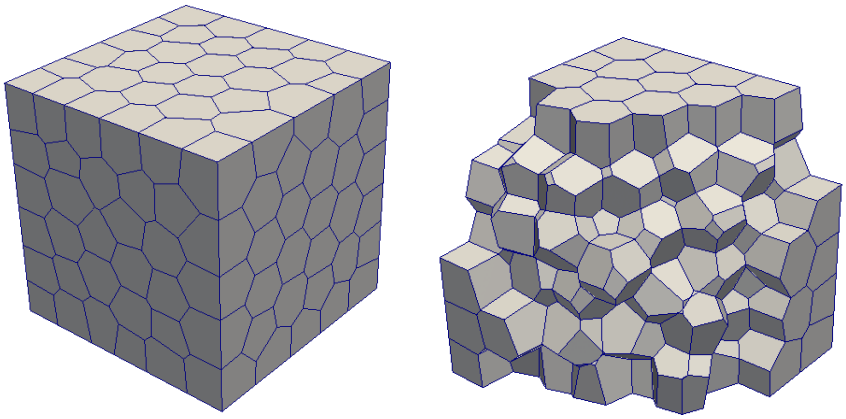

(a) (b)

Figure 7: Cube domain discretized with polyhedral elements. Representative mesh containing 200 polyhedra.

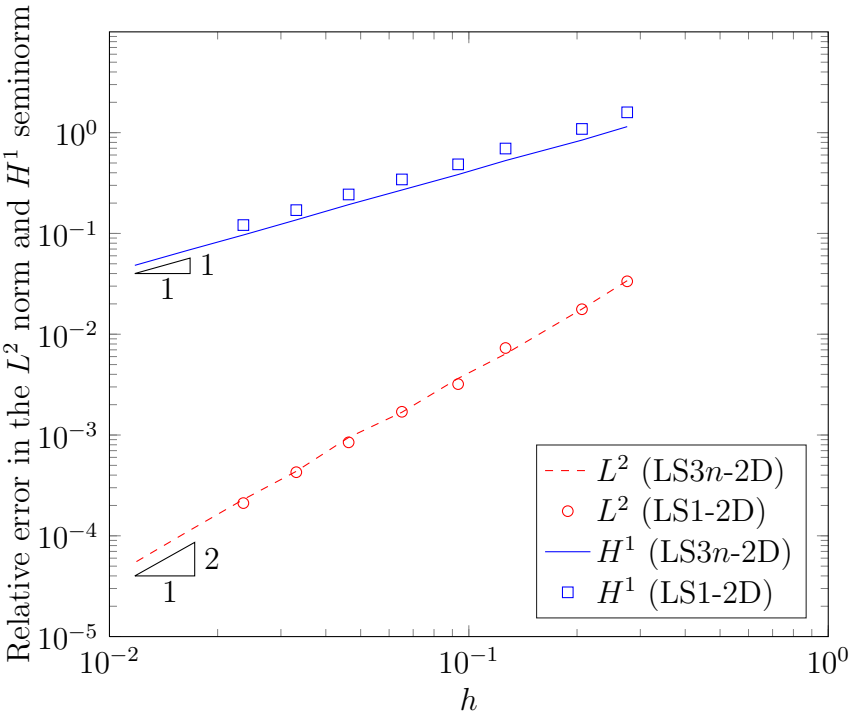

(a) Two dimensional domain

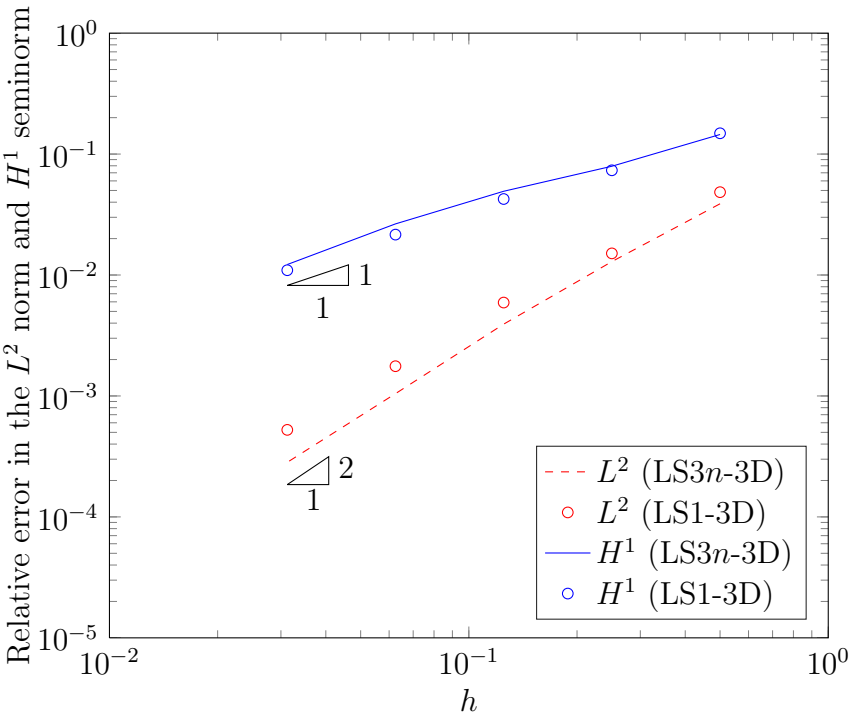

(b) Three dimensional domain

Figure 8: Convergence results for the quadratic patch test. The domain is discretized with arbitrary polytopes. The new integration scheme delivers optimal convergence rates in both the L^2 norm and H^1 seminorm with three times as many integration points per element as the standard approach.

5.1 Thick cantilever beam under end shear

In this example, a two-dimensional cantilever beam subjected to a parabolic shear load at the free end is examined, as shown in Figure 9a. The geometry of the cantilever is $L = 10$ m and $D = 2$ m. The material properties are: Young's modulus, $E = 3{\times}10^7$ N/m^2, Poisson's ratio $\nu = 0.25$ and the parabolic shear force is $P = 150$ N. The exact solution for the displacement field is given by [47]:

$$
\begin{aligned}
u(x,y) &= \frac{Py}{6EI}\left[(9L-3x)x + (2+\nu)\left(y^2 - \frac{D^2}{4}\right)\right], \\
v(x,y) &= -\frac{P}{6EI}\left[3\nu y^2(L-x) + (4+5\nu)\frac{D^2 x}{4} + (3L-x)x^2\right].
\end{aligned} \tag{36}
$$

where $I = D^3/12$ is the second area moment. A state of plane stress is considered. Figure 9b shows a sample polygonal mesh. The numerical convergence of the relative error in the L^2 norm and the H^1 seminorm is shown in Figure 10. It can be seen that the proposed one point integration rule yields optimal convergence rate in both the L^2 norm and the H^1 seminorm. With mesh refinement the solution approaches the analytical solution asymptotically. It is further noted that the proposed integration rule yields similar results when compared to the recently proposed integration rule [18] that employs $3n$ integration point per element (see Figure 5a).

5.2 Three dimensional cantilever beam under end torsion

Consider a prismatic cantilever beam with $\Omega : [-1,1] \times [-1,1] \times [0,L]$ (see Figure 11 (a) for geometry of the domain) subjected to end torsion. The material is assumed to be homogeneous and isotropic with Youngs' modulus, $E = 1$ N/m^2, Poisson's ratio $\nu = 0.3$ and shear modulus $G = E/(2(1+\nu))$. Two different loading conditions, viz., end shear load and end torsion, are considered here for which analytical solutions are available in the literature. The accuracy and the convergence properties are studied for random closed-pack Voronoi mesh. Figure 12 shows a few representative random Voronoi meshes employed for this study. The exact displacement solution for this boundary value problem is [1]:

$$
\begin{aligned}
u_x &= -\beta yz \\
u_y &= \beta xz \\
u_z &= \beta\left[xy + \sum_{n=1}^{\infty} \frac{32a^2(-1)^n}{\pi^3(2n-1)^3} \sin\left((2n-1)\frac{\pi x}{2a}\right) \frac{\sinh((2n-1)\frac{\pi y}{2a})}{\cosh((2n-1)\frac{\pi y}{2a})}\right]
\end{aligned} \tag{37}
$$

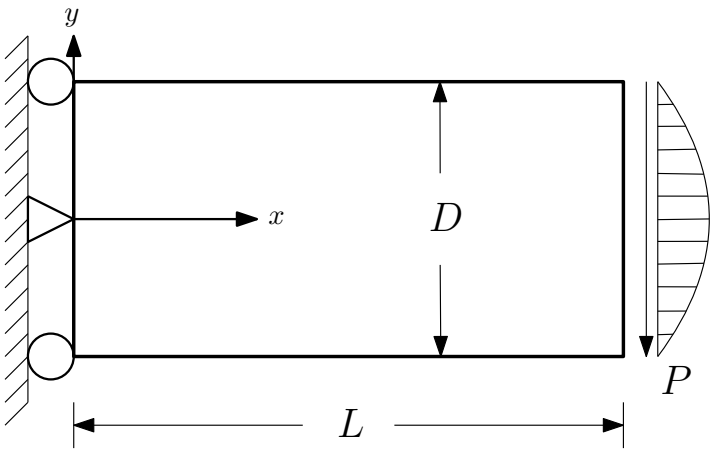

(a)

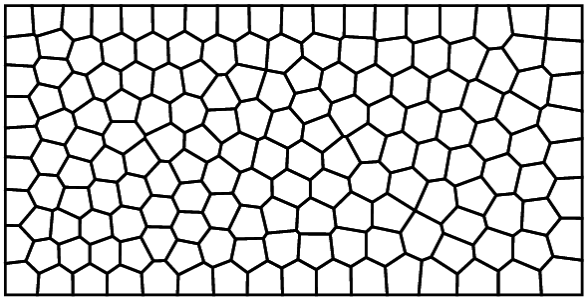

(b)

Figure 9: Two dimensional cantilever beam: (a) Geometry and boundary conditions and (b) representative polygonal mesh

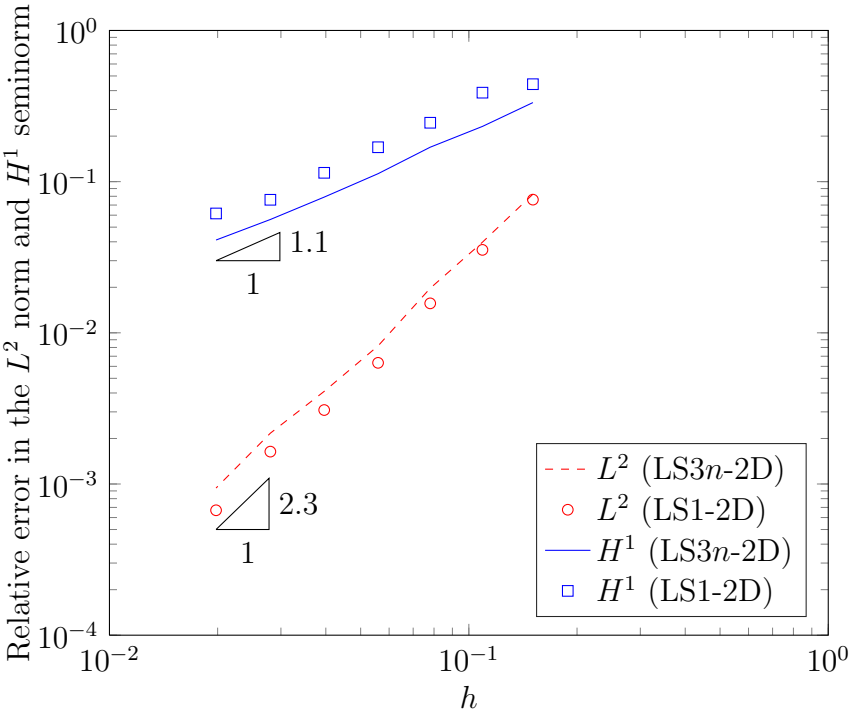

Figure 10: Convergence of the relative error in the L^2 norm and the H^1 seminorm with mesh refinement for a two-dimensional cantilever beam subjected to end shear. It is inferred that the proposed integration scheme yields optimal convergence rates.

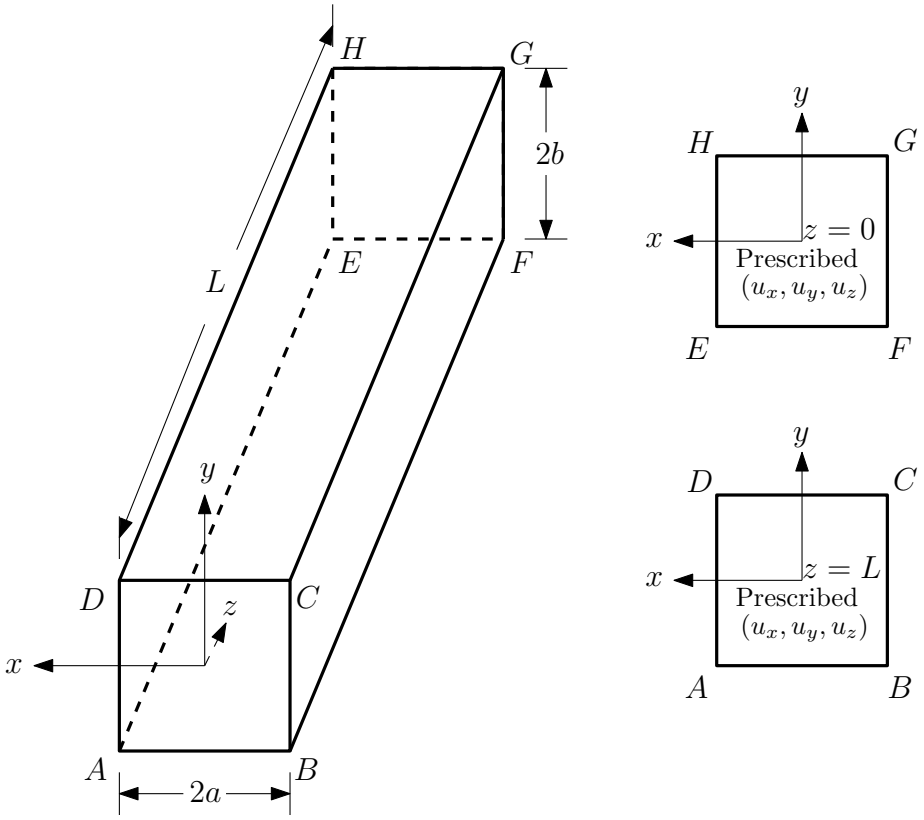

Figure 11: Cantilever beam: (a) Geometry, length L and rectangular cross-section of width $2a$ and height $2b$. For the present study, the following dimensions are considered: $L = 5$, $a = b = 1$.

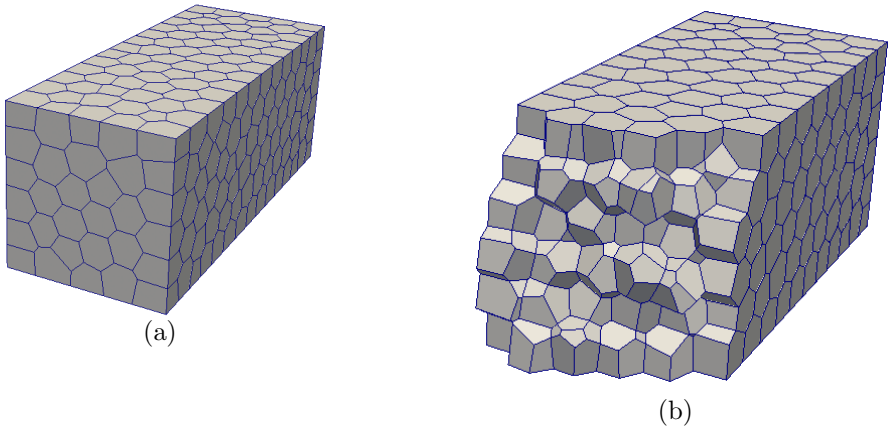

Figure 12: Three dimensional cantilever beam: representative polyhedral discretization.

where the constant β is proportional to the total torque applied to the beam. The exact Cauchy stress field is given by:

$$\begin{aligned}
\sigma_{xx} &= \sigma_{xy} = \sigma_{yy} = \sigma_{zz} = 0 \\
\sigma_{xz} &= G\beta \sum_{n=1}^{\infty} \frac{16a(-1)^n}{\pi^2(2n-1)^2} \cos\left((2n-1)\frac{\pi x}{2a}\right) \frac{\sinh((2n-1)\frac{\pi y}{2a})}{\cosh((2n-1)\frac{\pi y}{2a})} \\
\sigma_{yz} &= G\beta \left[2x + \sum_{n=1}^{\infty} \frac{16a(-1)^n}{\pi^2(2n-1)^2} \sin\left((2n-1)\frac{\pi x}{2a}\right) \frac{\cosh((2n-1)\frac{\pi y}{2a})}{\cosh((2n-1)\frac{\pi y}{2a})}\right]
\end{aligned} \tag{38}$$

For the present study, the infinite series in Equations (37) - (38) is truncated at $n = 40$ and analytical displacements are prescribed at $z = 0$ and at $z = L$. On the rest of the boundary, tractions are applied that are consistent with the exact stress field. The convergence of the proposed technique over arbitrary polyhedron with mesh refinement is studied. The results from the present approach is compared with the linear smoothing technique that employs 4 integration points per tetrahedron. The relative error in the L^2 norm and the H^1 seminorm is shown in Figure 13 and it can be seen that the proposed approach yields optimal convergence rates. Figure 14 shows the vector sum of the displacement and the von-Mises equivalent stress on the deformed shape for a representative polyhedral discretization.

5.3 Three dimensional L-shaped block

Consider a three dimensional square block with a cubic hole subjected to the surface traction, $\mathbf{t} = 1\text{N/mm}^2$ as shown in Figure 15a. Due to symmetry, only a quarter of the domain is modeled. This results in a three dimensional L-shaped block as shown in Figure 15b. The input parameters used for this analysis are $a = 50$mm, $E = 1$ MPa and $\nu = 0.3$. The reference solution (Strain energy = 382505 MPa) is computed using the commercial software Abaqus with an overkill finite element mesh (49211 tetrahedral elements). Figure 17 shows the convergence of the strain energy with mesh refinement. It is opined that the results from the proposed numerical integration scheme converges asymptotically to the reference solution. The rate of convergence is also shown in the inset. The oscillations that is seen could be attributed to the fact that the polyhedral mesh refinement is not structured.

5.4 Stress analysis of a femur

As a last example, we perform a stress analysis of a right human proximal femur. The computed tomography (CT) scan of a patient was obtained using General Electric's Ultrafast High-Resolution Multislice CT scanner (16 slices) containing 909 images with the pixel size of 0.7031 mm, slice thickness of 0.4 mm and resolution of 512×512. The Materialise's Interactive Medical Image Control System (MIMICS) is then used to segment the images with default thresholding range (226 HU and 3071 HU) to create

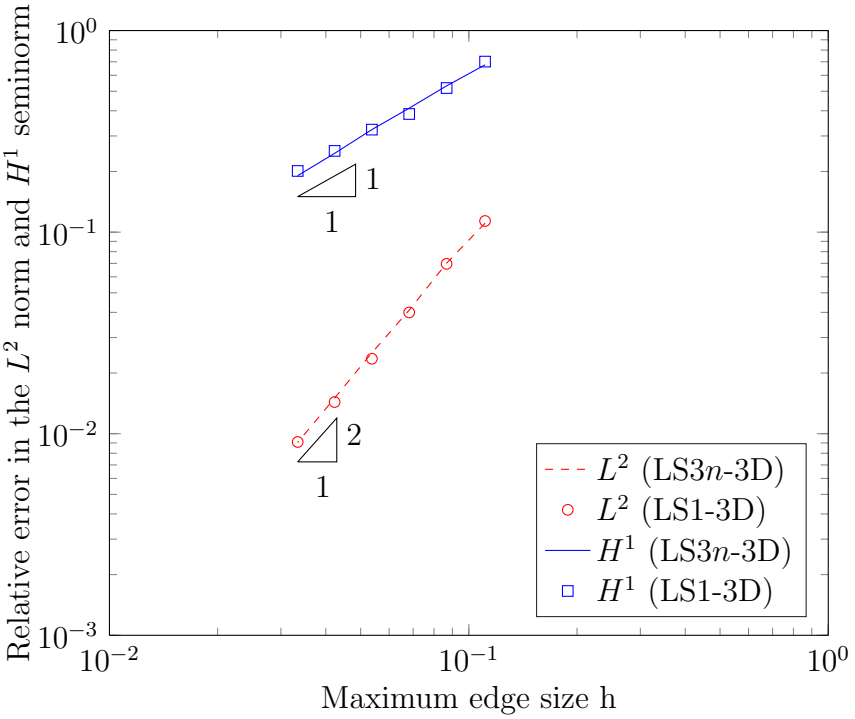

Figure 13: Convergence of the relative error in the L^2 norm and the H^1 seminorm with mesh refinement for the three-dimensional cantilever beam problem subjected to end torsion. It can be seen that the proposed integration rule yields similar results when compared to linear smoothing scheme with four integration points. The rate of convergence is also optimal in both the L^2 norm and in the H^1 seminorm.

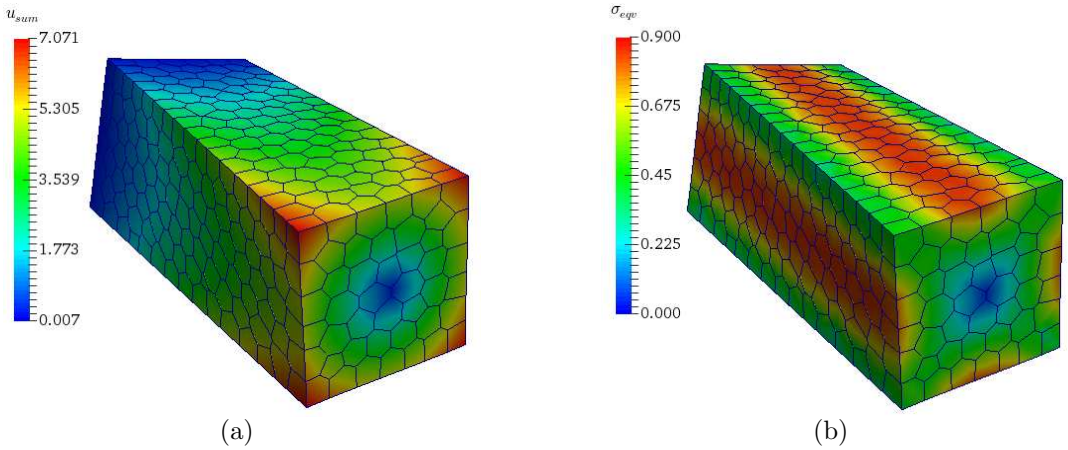

(a) (b)

Figure 14: Cantilever beam subjected to pure torsion: (a) vector sum of the displacements and (b) von-Mises equivalent stress

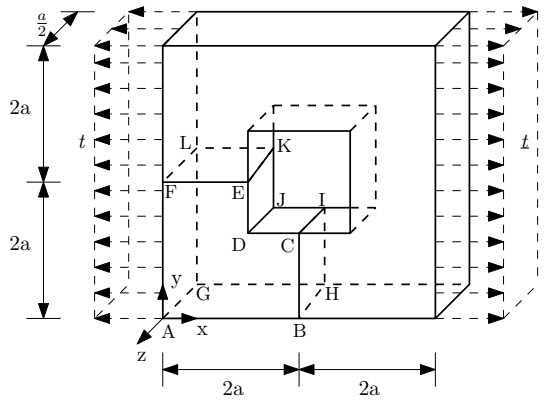

(a) A 3D block problem: Geometry and boundary conditions.

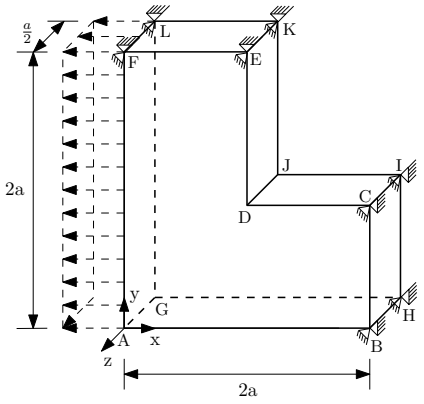

(b) An L-shaped quarter model: Geometry and boundary conditions.

Figure 15: Three dimensional block and an L-shaped quarter model.

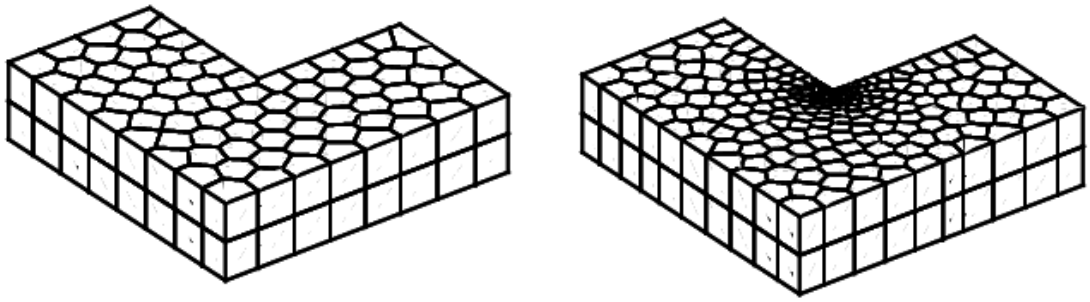

(a) (b)

Figure 16: Few sample meshes of L-shaped quarter model containing: a) 80 and b) 320 elements.

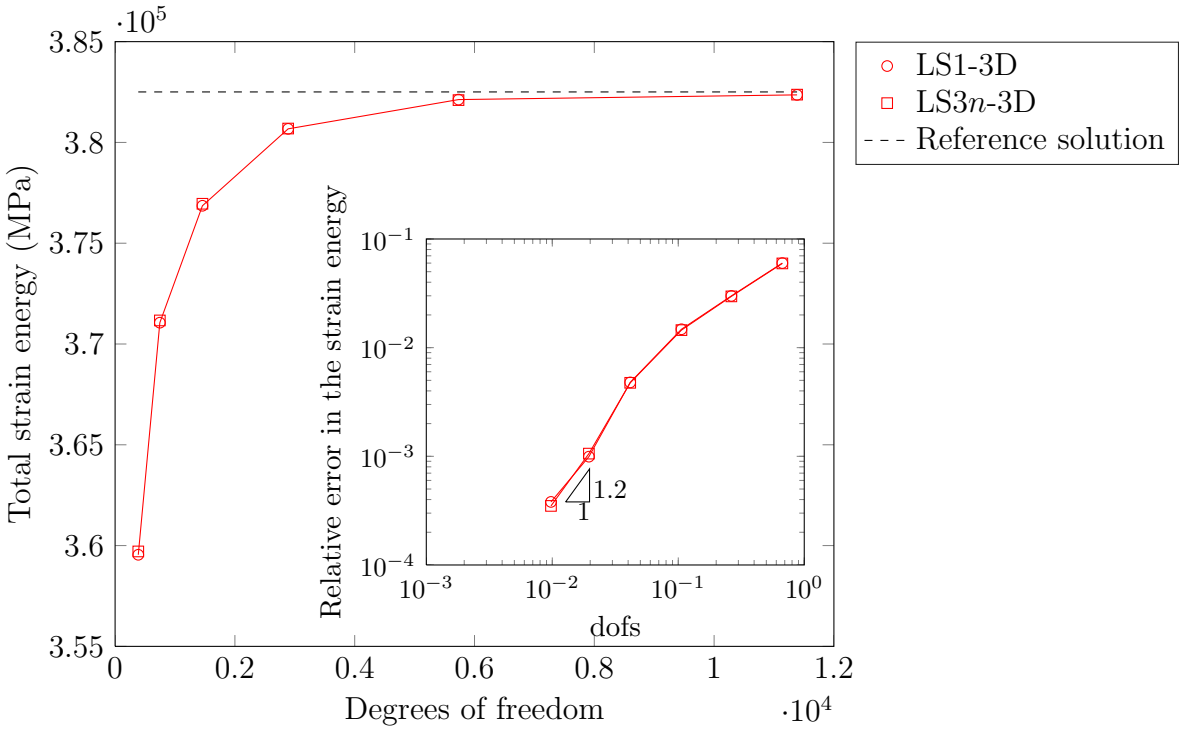

Figure 17: Three dimensional L-shaped block: Convergence of the strain energy with mesh refinement. The rate of convergence is shown in the inset.

three-dimensional model. The femur is then discretized with polyhedral elements using geogram. The total length of the femur is 288.48 mm. Figure 18 shows the geometry and the boundary conditions employed in this study. As shown, the displacement on the bottom face of the femur is restrained in all three directions and a displacement of magnitude 0.1 is prescribed in the negative z-direction at all the nodes whose $z-$coordinate is greater than 281.79mm. The femur is assumed to be linear isotropic with Young's modulus, $E = 15$ GPa and Poisson's ratio, $\nu = 0.3$. The reference solution for the strain energy is obtained using the commercial FE software, Abaqus with 33,5168 tetrahedral elements. Figure 19 shows the convergence of the strain energy with mesh refinement with the proposed numerical integration technique. It is seen that the results from the proposed technique converge to the reference solution asymptotically. Figure 20 shows the von-Mises equivalent stress contour plot for a typical polyhedral discretization.

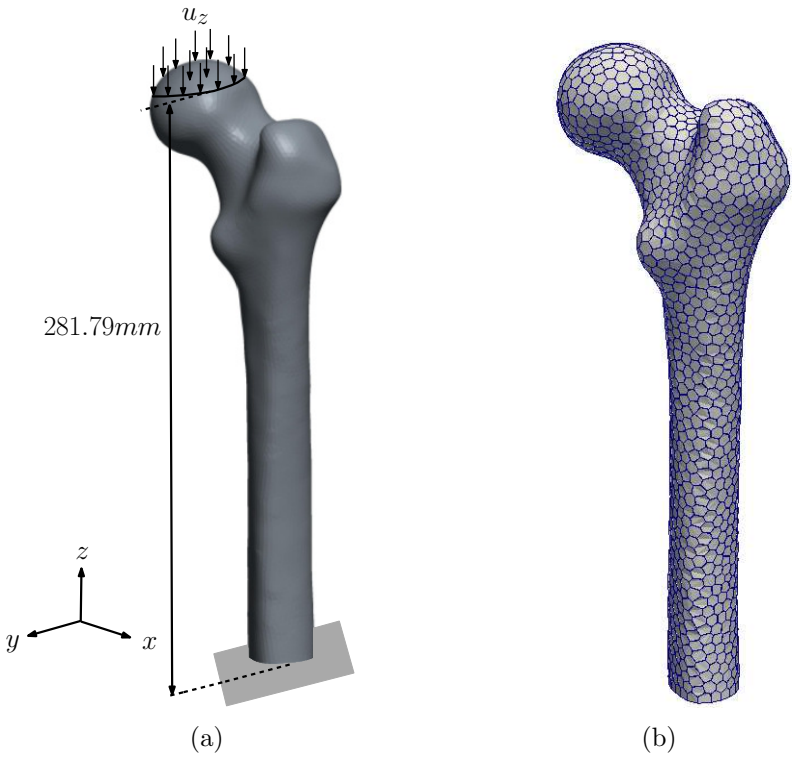

Figure 18: Human femur: (a) geometry and boundary conditions and (b) representative polyhedral mesh.

6 Concluding Remarks

A linearly consistent one point quadrature rule has been proposed to integrate over star convex arbitrary polytopes. The results from the proposed scheme are compared with the linear smoothing scheme. The linear smoothing scheme (denoted as LS3n-2D/LS3n-

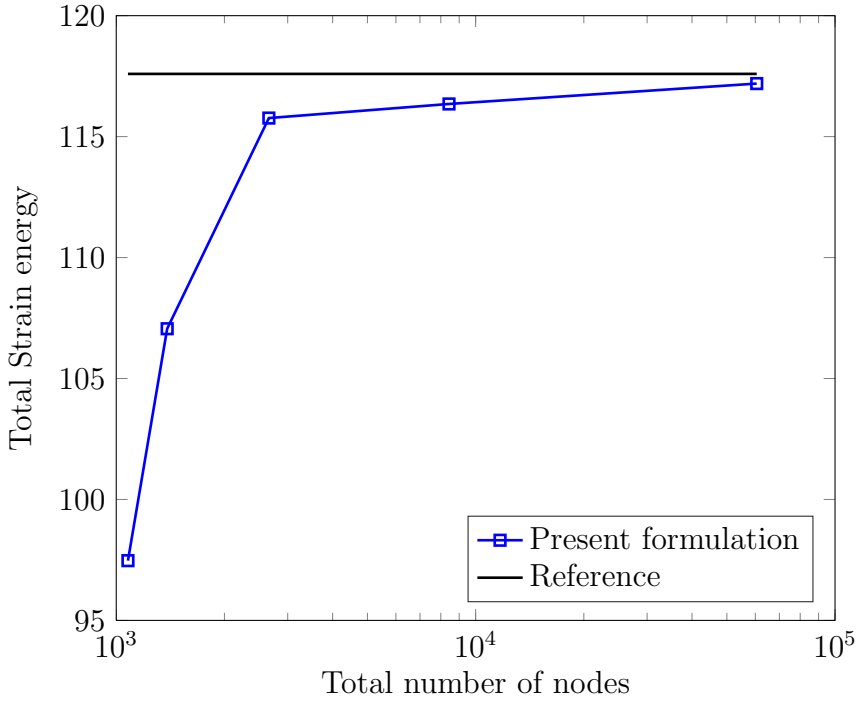

Figure 19: Convergence of the total strain energy with mesh refinement for a femur.

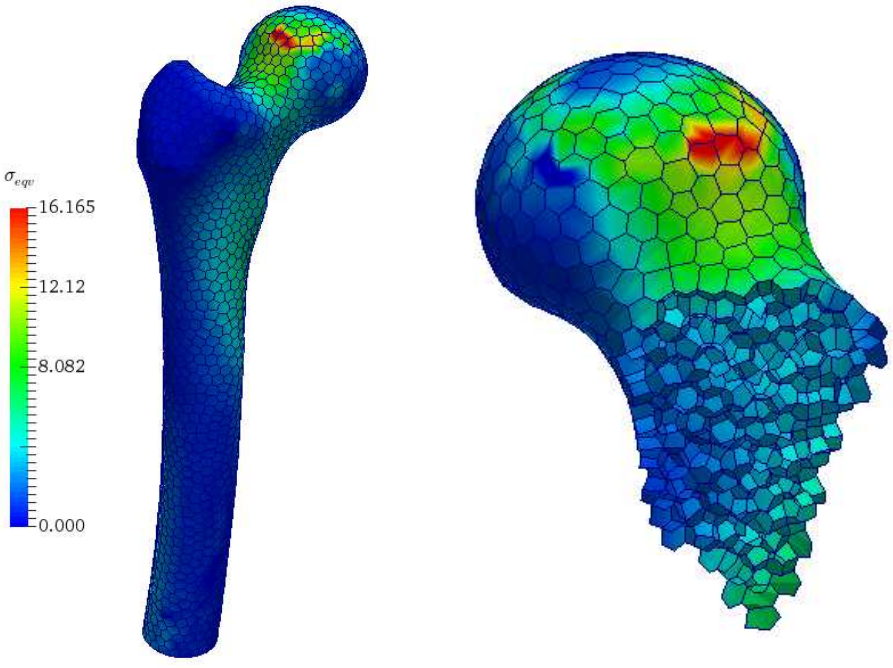

(a) (b)

Figure 20: von Mises equivalent stress contour for a femur.

3D in the paper) consists in subdividing the poly-element into simplices (triangles or tetrahedra). The linear smoothing scheme is then performed over each triangle. This process requires $3n$ and $4n$ integration points per element, where n is the number of sides/faces of the element. This significantly reduces the computational effort whilst preserving accuracy and stability. The proposed integration rule also preserves optimal convergence rates in both the L^2 norm and in the H^1 seminorm.

Acknowledgements

Stéphane Bordas thanks the financial support of the European Research Council Starting Independent Research Grant (ERC Stg grant agreement No. 279578) entitled "Towards real time multiscale simulation of cutting in non-linear materials with applications to surgical simulation and computer guided surgery" and is also grateful for the support of the Fonds National de la Recherche Luxembourg FNRS-FNR grant INTER/FNRS/15/11019432/EnLightenIt/Bordas.

References

References

[1] J Barber. *Elasticity*. Springer, New York, 2010.

[2] S. O. R. Biabanaki and A. R. Khoei. A polygonal finite element method for modeling arbitrary interfaces in large deformation problems. *Computational Mechanics*, 50(1):19–33, 2012.

[3] S.O.R. Biabanaki, A. R. Khoei, and P. Wriggers. Polygonal finite element methods for contact-impact problems on non-conformal meshes. *Computer Methods in Applied Mechanics and Engineering*, 269(1):198–221, 2014.

[4] J.E. Bishop. A displacement based finite element formulation for general polyhedra using harmonic shape function. *International Journal for Numerical Methods in Engineering*, 97:1–31, 2013.

[5] Mario Botsch, Mark Pauly, Leif Kobbelt, Pierre Alliez, Bruno Lévy, Stephan Bischoff, and Christian Röossl. Geometric modeling based on polygonal meshes. *https://hal.inria.fr/inria-00186820*, 47(2):441–453, 2007.

[6] Adrian Bowyer. Computing dirichlet tessellations. *Comput. J.*, 24(2):162–166, 1981.

[7] A. Cangiani, E. H. Georgoulis, and P. Houston. hp-version discontinuous galerkin methods on polygonal and polyhedral meshes. *Mathematical Models and Methods in Applied Sciences*, 24(10):2009–2041, september 2014.

[8] J. S. Chen, C.T. Wu, S. Yoon, and Y. You. A stabilized conforming nodal integration for galerkin mesh-free methods. *International Journal for Numerical Methods in Engineering*, 50(2):435–466, 2001.

[9] L Beirao da Veiga, F Brezzi, A Cangiani, G Manzini, L D Marini, and A Russo. Basic principles of virtual element methods. *Mathematical Models and Methods in Applied Sciences*, 23:199–214, 2013.

[10] L. Beirao da Veiga, F. Brezzi, L. D. Marini, and A. Russo. The hitchhiker's guide to the virtual element method. *Mathematical Models and Methods in Applied Sciences*, 24(08):1541–1573, July 2014.

[11] L Beirao da Veiga and G Manzini. The mimetic finite difference method and the virtual element method for elliptic problems with arbitrary regularity. Technical Report LA-UR-12-22977, Los Alamos National Laboratory, 2012.

[12] KY Dai, GR Liu, and TT Nguyen. An n-sided polygonal smoothed finite element method (nsfem) for solid mechanics. *Finite Elements in Analysis and Design*, 43:847–860, 2007.

[13] J. Droniou. Finite volume schemes for diffusion equation: Introduction to and review of modern methods. *Mathematical Models and Methods in Applied Sciences*, 24:1575–1619, 2010.

[14] Qiang Du, Vance Faber, and Max Gunzburger. Centroidal voronoi tessellations: Applications and algorithms. *SIAM Rev.*, 41(4):637–676, December 1999.

[15] Q. Duan, X. Gao, B. Wang, X. Li, and H. Zhang. A four-point integration scheme with quadratic exactness for three-dimensional element-free galerkin method based on variationally consistent formulation. *Computer Methods in Applied Mechanics and Engineering*, 280(1):84–116, 2014.

[16] Q. Duan, X. Gao, B. Wang, X. Li, H. Zhang, T. Belytschko, and Y. Shao. Consistent element-free galerkin method. *International Journal for Numerical Methods in Engineering*, 99(2):79–101, 2014.

[17] M. S. Floater. Mean value coordinates. *Computer Aided Geometric Design*, 20(1):19–27, 2003.

[18] A. Francis, A.Ortiz-Bernardin, S. P. A. Bordas, and S. Natarajan. Linear smoothed polygonal and polyhedral finite elements. *International Journal for Numerical Methods in Engineering*, 109(9):1263–1288, 2017.

[19] Arun. Gain. *Polytope-based topology optimization using a mimetic-inspired method*. PhD thesis, University of Illinois at Urbana-Champaign, 2014.

[20] X. Gao, Q. Duan, Y. Shao, X. Li, B. Chen, and H. Zhang. Quadratically consistent one-point (qc1) integration for three-dimensional element-free galerkin method. *Finite Elements in Analysis and Design*, 114:22–38, 2016.

[21] Xu hai Tang, Sheng-Chuan Wu, Chao Zheng, and Jian hai Zhang. A novel virtual node method for polygonal elements. *Applied Mathematics and Mechanics*, 30:1233–1246, 2009.

[22] J. Jaskowiec, P. Plucinski, and A. Stankiewicz. Discontinuous galerkin method with arbitrary polygonal finite elements. *Finite Elements in Analysis and Design*, 120:1–17, 2016.

[23] K. Jayabal, A. Menzel, A. Arockiarajan, and S.M Srinivasan. Micromechanical modelling of switching phenomena in polycrystalline piezoceramics. application of a polygonal finite element approach. *Computational Mechanics*, 48(4):421–435, 2011.

[24] A. R. Khoei, R. Yasbolaghi, and S.O.R. Biabanaki. A polygonal finite element method for modeling crack propogation with minimum remeshing. *International Journal of Fracture*, 194(2):123–148, 2015.

[25] Bruno Lévy. Robustness and efficiency of geometric programs: The predicate construction kit (PCK). *Computer-Aided Design*, 72:3–12, 2016.

[26] K. Lipnikov and G. Manzini. A high-order mimetic method on unstructured polyhedral mesh for the diffusion equation. *Journal of Computational Physics*, 272(1):360–385, September 2014.

[27] Yang Liu, Wenping Wang, Bruno Lévy, Feng Sun, Dong-Ming Yan, Lin Lu, and Chenglei Yang. On centroidal voronoi tessellation - energy smoothness and fast computation. *ACM Trans. Graph.*, 28(4):101:1–101:17, 2009.

[28] Stuart P. Lloyd. Least squares quantization in pcm. *IEEE Transactions on Information Theory*, 28:129–137, 1982.

[29] Paul Milgrom and Ilya Segal. Envelope Theorems for Arbitrary Choice Sets. *Econometrica*, 70(2):583–601, March 2002.

[30] S. Natarajan, E. T. Ooi, I. Chiong, and C. Song. Convergence and accuracy of displacement based finite element formulation over arbitrary polygons: Laplace interpolants, strain smoothing and scaled boundary polygon formulation. *Finite Elements in Analysis and Design*, 85:101–122, 2014.

[31] Sundararajan Natarajan, Stephane P. A. Bordas, and D. Roy Mahapatra. Numerical integration over arbitrary polygonal domains based on schwarz-christoffel conforming mapping. *International Journal for Numerical Methods in Engineering*, 80(1):103–134, 2009.

[32] Sundararajan Natarajan, Ean Tat Ooi, Albert Saputra, and Chongmin Song. A scaled boundary finite element formulation over arbitrary faceted star convex polyhedra. *Engineering Analysis with Boundary Elements*, 80:218–229, 2017.

[33] Sundararajan Natarajan, Ean Tat Ooi, and Chongmin Song. Finite element computations over quadtree meshes: strain smoothing and semi-analytical formulation.

International Journal of Advances in Engineering Sciences and Applied Mathematics, 7(3):124–133, 2015.

[34] Son Nguyen-Hoang and H. Nguyen-Xuan. A polytree-based adaptive polygonal finite element for topology optimization: on an adaptive polytree mesh structure for topology optimization. *International Journal for Numerical Methods in Engineering*, 110(10):972–1000, 2016.

[35] E. Ooi, C. Song, and S. Natarajan. Construction of high-order complete scaled boundary shape functions over arbitrary polygons with bubble functions. *International Journal for Numerical Methods in Engineering*, 108(9):1086–1120, 2016.

[36] Alexander Rand, Andrew Gillette, and Chandrajit Bajaj. Quadratic serendipity finite elements on polygons using generalized barycentric coordinates. *Mathematics of Computation*, 83:2691–2716, February 2014.

[37] Hang Si. Tetgen, a delaunay-based quality tetrahedral mesh generator. *ACM Trans. Math. Softw.*, 41(2):11:1–11:36, 2015.

[38] A. Sommariva and M. Vianello. Product gauss cubature over polygons based on green's integration formula. *BIT Numerical Mathematics*, 47(2):441–453, 2007.

[39] N. Sukumar. Construction of polygonal interpolants: a maximum entropy approach. *International Journal for Numerical Methods in Engineering*, 61(12):2159–2181, 2004.

[40] N. Sukumar and E. A. Malsch. Recent advances in the construction of polygonal finite element interpolants. *Archives of Computational Methods in Engineering*, 13(1):129–163, 2006.

[41] N. Sukumar and A. Tabarrei. Conforming polygonal finite elements. *International Journal for Numerical Methods in Engineering*, 61:2045–2066, 2004.

[42] N. Sukumar and A. Tabarrei. Polygonal interpolants: Construction and adaptive computations on quadtree meshes. *European Congress on Computational methods in applied sciences and engineering*, pages 24–28, July 2004.

[43] K.Y Sze and N. Sheng. Polygonal finite element method for nonlinear constitutive modeling of polycrystalline ferroelectrics. *Finite Elements in Analysis and Design*, 42(2):107–129, November 2005.

[44] C. Talischi and G. H. Paulino. Addressing integration error for polygonal finite elements through polynomial projections: A patch test connection. *Mathematical Models and Methods in Applied Sciences*, 24(8):1701–1727, 2014.

[45] Cameron Talischi, Glaucio H Paulino, Anderson Pereira, and Ivan FM Menezes. Polytop: a Matlab implementation of a general topology optimization framework using unstructured polygonal finite element meshes. *Struct. Multidisc Optim*, 45:329–357, 2012.

[46] Cameron Talischi, Anderson Pereira, Glaucio H. Paulino, Ivan F. M. Menezes, and Marcio S. Carvalho. Polygonal finite elements for incompressible fluid flow. *International Journal for Numerical Methods in Engineering*, 74(2):134–151, 2014.

[47] S. Timoshenko and J. N. Goodier. *Theory of Elasticity*, volume 3rd edition. McGraw-Hill, 1970.

[48] J. Warren. On the uniqueness of barycentric coordinates. In *Proceedings of AGGM02*, pages 93–99, 2003.

[49] J. Warren, S. Schaefer, A. Hirani, and M. Desbrun. Barycentric coordinates for convex sets. *Advances in Computational Mechanics*, 27(3):319–338, 2007.

[50] David Watson. Computing the n-dimensional delaunay tessellation with application to voronoi polytopes. *Comput. J.*, 24(2):167–172, 1981.

[51] Dong-Ming Yan, Wenping Wang, Bruno Lévy, and Yang Liu. Efficient computation of clipped voronoi diagram for mesh generation. *Computer-Aided Design*, 45(4):843–852, 2013.